Modeling of the phase transformation of germanate olivine by using the phase-field method

Sando Sawa[1]*, Jun Muto[1], Hiroyuki Nagahama[1]

[1]Department of Earth Science, Tohoku University, Sendai, Miyagi, Japan

Key Points:

- Germanate olivine (α)-spinel (γ) phase transformation was modeled by phase field method.
- The shear plastic strain affects the grain growth and the grain shape of spinel (γ) phase.
- The shapes of anticracks and nano shear bands composed of nanocrystalline spinel are affected by large elastic strain energy.

*Sendai, Miyagi, Japan

Corresponding author: Sando Sawa, sando.sawa.t1@dc.tohoku.ac.jp

Abstract

Olivine is the main constituent of the upper mantle, and its phase transformation affects the rheology of the subduction zone. It is crucial to reveal the kinetics of olivine (α)-spinel (γ) phase transformation under differential stress. To investigate the effect of microstructural properties on phase transformations such as grain boundary energy and plastic strain, we conducted a phase-field simulation using germanate olivine, an analog of silicate olivine. We conducted the simulations under various confining pressures of 1-5 GPa, temperatures of 1000 and 1200 K, with/without plastic strain, and various grain boundary energy. Under static conditions, the volume fraction of the γ phase increases as the overpressure increases because the chemical-free energy promoting grain growth dominates over the elastic strain energy, inhibiting grain growth. Under differential stress, at a slight overpressure, the volume fraction of the γ phase increases proportion to the chemical-free energy's magnitude. Meanwhile, at a significant overpressure, the γ phase's volume fraction decreases due to the sizeable elastic strain energy. Furthermore, the volume fraction of the γ phase under differential stress is more significant than under static conditions due to the considerable shear plastic strain. The grains of the γ phase under differential stress at low confining pressure are lens-shaped with a strong preferred orientation normal to the maximum compression direction because of the shear plastic strain. Meanwhile, the grains of the γ phase at a high confining pressure are ultra-thin because of the considerable elastic strain energy.

Plain Language Summary

Olivine is the most abundant mineral in the upper mantle and undergoes phase transformation to wadsleyite (β phase) and ringwoodite (γ phase). This phase transformation under differential stress is essential as one of the causes of deep-focus earthquakes and slab bending. However, the effect of microstructural properties, such as plastic strain, on the transformation under differential stress has not yet been revealed. Therefore, we conducted a phase-field simulation to simulate microstructure evolution and set microstructural properties. We used germanate olivine, an analog of silicate olivine, to compare our results with a previous study using germanate olivine, and modeled the grain growth of the germanate γ phase. As a result, plastic strain promotes grain growth in the γ phase. At low confining pressure, the evolution of shear plastic strain is substantial, and the γ grains are lens-shaped normal to the maximum compression direction, similar to "an-

ticracks" reported by the previous deformation experiment. At a high confining pressure, the elastic strain energy inhibiting the grain growth, the γ grains are ultra-thin, similar to the nano-shear bands composed of nanocrystalline γ grains reported by the previous deformation experiment.

1 Introduction

Olivine, the main constituent of the upper mantle, undergoes phase transformation to wadsleyite at 410 km depth and ringwoodite at about 520 km (Akaogi et al., 1989). Its phase transformation affects mantle rheology, especially inside slabs, because its rheology is influenced by the physicochemical properties of the mineral phases (Rubie, 1984; Karato et al., 2001; Yamazaki et al., 2005; Kubo et al., 2009; Tajima et al., 2015; Ishii & Ohtani, 2021). The viscosity of mantle minerals in the cold slab can be reduced by grain size reduction associated with the olivine-wadsleyite/ringwoodite (spinel) phase transformation, leading to the domination of diffusion creep (Vaughan & Coe, 1981; Karato et al., 2001). Furthermore, the phase transformation is presumed to be one of the mechanisms responsible for deep-focus earthquakes (e.g., Green et al., 1990; Burnley et al., 1991; Tingle et al., 1993; Schubnel et al., 2013; Wang et al., 2017; Zhan, 2017). In addition, shear instability can occur at the fine-grained spinel phase nucleated by the phase transformation of metastable olivine in the subducting slab (Ogawa, 1987; Hobbs & Ord, 1988; Karato et al., 2001; Meng et al., 2014; Zhan et al., 2014; Zhan, 2017). Therefore, it is important to reveal the kinetics of the olivine-spinel phase transformation under differential stress to understand better its role in the rheology of the subduction zone.

Two mechanisms of olivine-wadsleyite/ringwoodite ($\alpha \rightarrow \beta/\gamma$) phase transformation have been proposed: intracrystalline nucleation and nucleation at the grain boundary (e.g., Vaughan et al., 1982; Boland & Liu, 1983; Kerschhofer et al., 1996, 1998, 1998; Dupas-Bruzek et al., 1998). The intracrystalline nucleation has the following four stages: (1) $(100)_\alpha$ stacking faults form in olivine crystals, (2) thin ringwoodite platelets nucleate on these stacking faults coherently; (3) the platelets grow semi-coherently; and (4) ringwoodite/wadsleyite nucleate at the platelet interfaces incoherently (Kerschhofer et al., 2000). Nucleation at the grain boundary is an incommensurate transformation and has two cases: (1) the nucleation rate is fast relative to the growth rate, and (2) the nucleation rate is slow relative to the growth rate (Brearley et al., 1992). Burnley (1995) suggested that the growth rate of the transformed grains at the grain boundary were in-

sensitive to pressure, whereas the intracrystalline nucleation affected the rate of the transformation at high pressure because intracrystalline nucleation tended to occur at high pressure. However, previous studies have not referred to the effect of microstructural properties on the grain growth rate of the phase transformation, such as the grain boundary energy and plastic strain derived from the transformation and deformation. To reveal the effect, it is useful to conduct numerical experiments capable of controlling and evaluating various parameters freely.

We adopted the phase-field method (PFM) to simulate the phase transformation using a diffuse phase model (Fix, 1983). In the PFM, we set the order parameter that describes the continuous distribution of two phases, and the phase boundary is described as a field where the order parameter continuously changes between two phases (e.g., Chen & Khachaturyan, 1991; Steinbach & Pezzolla, 1999). Therefore, PFM is a powerful tool for the simulation of microstructural evolution with complex morphological features such as dendrites (Wheeler et al., 1993; Shimokawabe et al., 2011; Yang et al., 2021), martensite microstructure after phase transformation (Yamanaka et al., 2008, 2010; Yeddu et al., 2012), dynamic and static recrystallization (Takaki et al., 2008; Takaki & Tomita, 2010), and crack propagation (Miehe et al., 2015; Schneider et al., 2016; Evans et al., 2020).

Although experiments must be conducted under relevant conditions for the olivine-spinel phase boundary within the subducting slab, many previous experiments have been conducted using germanate olivine (Mg_2GeO_4) (e.g., Vaughan & Coe, 1981; Weidner & Hamaya, 1983; Green et al., 1990; Burnley et al., 1991; Dupas-Bruzek et al., 1998; Schubnel et al., 2013; Wang et al., 2017; Sawa, Muto, et al., 2021; Sawa, Miyajima, et al., 2021). This is because it is challenging to conduct deformation experiments on silicate olivine under such extreme conditions. Germanate olivine has only α and γ phases, and no β phase, unlike silicate olivine. However, it can undergo phase transformation at a much lower pressure than that of silicate olivine, and the physical and mineralogical properties are similar (Weidner & Hamaya, 1983). Burnley et al. (1991) conducted deformation experiments of germanate olivine using a Griggs-type deformation apparatus at a low confining pressure of 1-2 GPa and proposed that faulting occurred along lens-shaped grains of germanate γ phase ("anticracks") with a strong preferred orientation normal to the maximum compression. Anticracks are filled with nanocrystalline aggregates of germanate olivine (Burnley et al., 1991; Green, 2007). Meanwhile, Schubnel et al. (2013) and Wang et al. (2017) also conducted deformation experiments on germanate olivine

using a D-DIA apparatus at a higher confining pressure of 2-5 GPa than that in Burnley et al. (1991). They proposed that transformational faulting occurred on nano shear bands comprising fine-grained γ grains, which were different from those in Burnley et al. (1991). Its phase transformation is an exothermic phenomenon; hence, the formation of new γ grains releases a small amount of heat that produces a slight increase in local temperature, leading to an increase in the local nucleation rate of the γ phase (Green, 2007). Simultaneously, the negative volume change of the $\alpha \rightarrow \gamma$ phase transformation causes the nucleation of the γ phase owing to compressive hoop stresses that increase the driving force for the nucleation of additional crystals (Green, 2007). Majewski and Teisseyre (1998) described the microphysics of anticrack formation using a theory of antidislocation leading to the faulting for the deep-focus earthquakes. However, they hardly referred to how anticracks formed with a strong preferred orientation normal to the maximum compression direction and the difference in the form of γ phase derived from a confining pressure. Furthermore, a comparison of our results with those of two previous experiments conducted under different pressures (Burnley et al., 1991; Schubnel et al., 2013; Wang et al., 2017) shows the robustness of our simulations.

In this study, we simulated the growth of the γ phase nucleated at the grain boundary when the nucleation rate is slow relative to the growth rate because the PFM method cannot simulate nucleation. Thus, we introduced the initial γ grains in advance. First, we constrained the grain boundary mobility in the magnesium germanate system required for the simulation. Because the mobility has not yet been determined experimentally, we conducted numerical experiments under identical conditions to those of previous experiments in which the growth rate of the γ phase has already been clarified (Burnley et al., 1991; Burnley, 1995). We then determined the grain boundary mobility by comparing the grain area of the γ phase in these simulations with that calculated from the growth rate of the γ phase in previous studies. Second, we simulated the phase transformation under various conditions of pressure, temperature, grain boundary energy, and plastic strain to reveal the microstructural growth kinetics of the $\alpha \rightarrow \gamma$ phase transformation and the difference in the formation conditions between anticracks at a low confining pressure and nano shear bands comprising fine-grained γ grains at a high confining pressure.

2 Model setting

2.1 Initial geometry

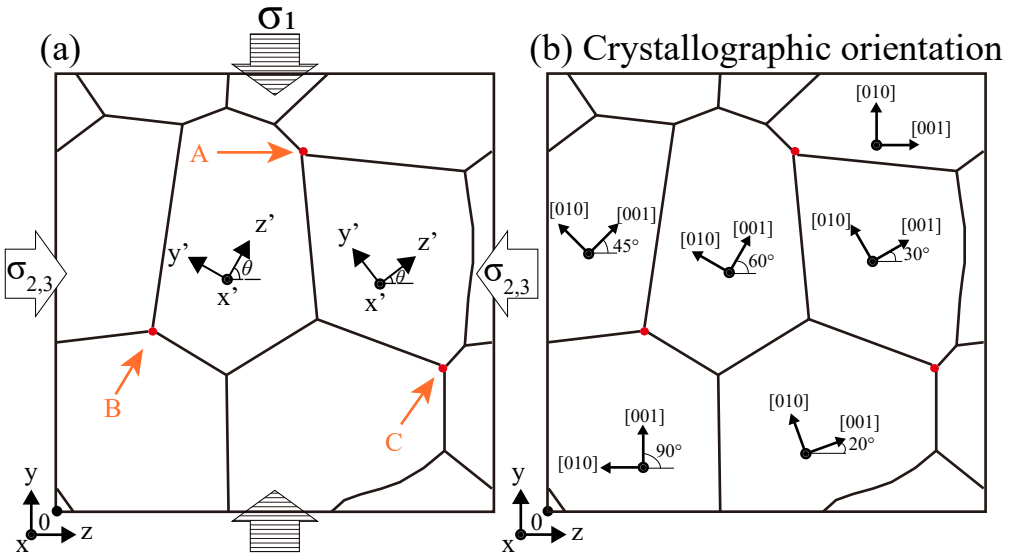

Figure 1. Geometry of the initial germanate olivine aggregate. The origin is the lower left of the aggregate. (a) θ and θ' show the angles of the α and γ phases between the global coordinate system (x-y-z) and the local coordinate system (x'-y'-z'), respectively. The initial nucleation sites of the γ phase are indicated by arrows A, B, and C. (b) The numbers show the crystallographic orientation of the α phase. The crystallographic orientations of the γ phase are 50° at position A, 25° at position B, and 75° at position C, respectively.

We set the geometry and coordinate system of the initial germanate olivine aggregates, as shown in Figure 1. γ grains were introduced in advance. The number of α and γ phase grains is six (white grains in Figure 1a) and 3 (small red grains shown by arrows A, B, and C in Figure 1a), respectively. For simplicity, we consider only the grains of the α phase with one crystallographic axes normally oriented to the plane. In this simulation, we adopted a periodic boundary condition under plane-strain conditions. The direction of the maximum principal compressive stress σ_1 is vertical (Line-filled arrows in Figure 1a), and the direction of the minimum principal stress $\sigma_{2,3}$ is horizontal (white arrows in Figure 1a). θ and θ' show the angles of the α and γ phases between the global coordinate system (x-y-z) and the local coordinate system (x'-y'-z'), respectively. Hence, θ and θ' represent the crystallographic orientations of the α and γ phases, respectively.

The crystallographic orientations of each grain in the α phase are shown in Figure 1b. The crystallographic orientations of the γ phase are 50° at position A, 25° at position B, and 75° at position C in Figure 1b, respectively.

2.2 Multi-Phase-Field method

For the olivine (α)-spinel (γ) transformation, we follow the multi-phase-field method proposed by Steinbach et al. (1996); Steinbach and Pezzolla (1999); Steinbach and Apel (2006); Takaki et al. (2009). Assuming that a polycrystalline system includes N grains (Figure 1), the phase field parameter is $\phi_i(r,t)$, where $i = 1, 2, \ldots, N, 0 \leq \phi_i \leq 1$. ϕ_i indicates the probability of the phase with the i-th crystal orientation at the position $\mathbf{r}$ and time t, and must satisfy $\sum_{i=1}^{N} \phi_i(\mathbf{r},t) = 1$. The evolution equation of ϕ_i is derived as follows (Steinbach & Pezzolla, 1999):

$$\frac{\partial \phi_i}{\partial t} = -\frac{2}{N} \sum_{j=1,\ j\neq i}^{N} M_{ij} \left\{ \sum_{k=1}^{N} \left[\frac{1}{2}(k_{ik} - k_{jk})\nabla^2 \phi_k + (W_{ik} - W_{jk})\phi_k \right] + \frac{\partial G^{(i)}}{\partial \phi_i} - \frac{\partial G^{(j)}}{\partial \phi_j} \right\}, \quad (1)$$

where M_{ij} is the phase-field mobility, k_{ij} is the gradient coefficient, W_{ij} is the height of the energy barrier, and $G^{(i)}$ is the Gibbs free energy of the i-th phase. This was developed from the phase-field method using a time-dependent Ginzburg-Landau equation assumed in irreversible thermodynamics (e.g. Fitts, 1962). The time-dependent Ginzburg-Landau equation has also been used in various fields (e.g., Lyakhovsky et al., 1993, 1997; Kawada et al., 2007; Muto et al., 2007). The first term in Eq. (1) indicates the gradient energy, and the fourth term is the penalty term that prohibits the growth of grains with different crystallographic orientations at the same place (Steinbach et al., 1996). In Eq. (1), we set M_{ij}, k_{ij}, and W_{ij} as the following matrices:

$$M_{ij} = \frac{\pi^2}{8\delta} \begin{pmatrix} 0 & M_0 & \cdots & M_0 \\ M_0 & 0 & & \vdots \\ \vdots & & \cdots & \vdots \\ M_0 & \cdots & \cdots & 0 \end{pmatrix}, \quad (2)$$

$$k_{ij} = \frac{8\delta}{\pi^2} \begin{pmatrix} 0 & \gamma_0 & \cdots & \gamma_0 \\ \gamma_0 & 0 & & \vdots \\ \vdots & & \cdots & \vdots \\ \gamma_0 & \cdots & \cdots & 0 \end{pmatrix}, \quad (3)$$

$$W_{ij} = \frac{4}{\delta}\begin{pmatrix} 0 & \gamma_0 & \cdots & \gamma_0 \\ \gamma_0 & 0 & & \vdots \\ \vdots & & \ddots & \vdots \\ \gamma_0 & \cdots & \cdots & 0 \end{pmatrix}. \tag{4}$$

Here, δ, M_0, and γ_0 are the grain boundary thickness, grain boundary mobility, and grain boundary energy, respectively. M_0 is calculated as follows:

$$M_0 = \frac{V_m D}{\delta R T}, \tag{5}$$

where V_m is the molar volume, D is the diffusivity of the atoms, R is the gas constant, and T is the absolute temperature (Hillert, 1975).

To consider the chemical energy G_{chem} and elastic energy G_{str}, we set

$$\frac{\partial G^{(i)}}{\partial \phi_i} - \frac{\partial G^{(j)}}{\partial \phi_j} = \left(\frac{\partial G_{chem}}{\partial \phi_i} + \frac{\partial G_{str}}{\partial \phi_i}\right) - \left(\frac{\partial G_{chem}}{\partial \phi_j} + \frac{\partial G_{str}}{\partial \phi_j}\right). \tag{6}$$

Eq. (6) indicates the difference in the Gibbs free energy potential (chemical energy potential + elastic energy potential) between the i-th and j-th grains. G_{chem} is often approximated by

$$\frac{\partial G_{chem}}{\partial \phi_i} - \frac{\partial G_{chem}}{\partial \phi_j} = -\frac{8}{\pi} E_{ij}\sqrt{\phi_i \phi_j}, \tag{7}$$

where E_{ij} is the driving force for the phase transformation, and $8/\pi$ is obtained from $\int_0^1 \sqrt{\phi_1\phi_2}d\phi = \int_0^1 \sqrt{\phi(1-\phi)}d\phi = \pi/8$ (Takaki et al., 2009). In Eq. (7), we set E_{ij} as the following matrix:

$$E_{ij} = \begin{pmatrix} 0 & \cdots & 0 & -E_0 & -E_0 & -E_0 \\ \vdots & \ldots & \vdots & -E_0 & -E_0 & -E_0 \\ 0 & \cdots & 0 & -E_0 & -E_0 & -E_0 \\ E_0 & E_0 & E_0 & 0 & \cdots & 0 \\ E_0 & E_0 & E_0 & \vdots & \ldots & \vdots \\ E_0 & E_0 & E_0 & 0 & \cdots & 0 \end{pmatrix}, \tag{8}$$

where E_0 is a constant corresponding to the driving force of the grain boundary migration between the i-th and j-th grains. Under the given external stress σ_{ij}^A, G_{str} is calculated as

$$G_{str} = \frac{1}{2V}\int_{\mathbf{r}} C_{ijkl}\varepsilon_{ij}^{el}(\mathbf{r})\varepsilon_{kl}^{el}(\mathbf{r})d\mathbf{r} - \sigma_{ij}^A \frac{1}{V}\int_{\mathbf{r}} \varepsilon_{ij}^c(\mathbf{r})d\mathbf{r} \tag{9}$$

$$= \frac{1}{2V}\int_{\mathbf{r}} C_{ijkl}\{\bar{\varepsilon}_{ij}^c + \delta\varepsilon_{ij}^c(\mathbf{r}) - \varepsilon_{ij}^0(\mathbf{r})\}\{\bar{\varepsilon}_{kl}^c + \delta\varepsilon_{kl}^c(\mathbf{r}) - \varepsilon_{kl}^0(\mathbf{r})\}d\mathbf{r} - \sigma_{ij}^A\bar{\varepsilon}_{ij}^c, \tag{10}$$

where C_{ijkl} is the elastic modulus of germanate olivine, $\bar{\varepsilon}^c_{ij}$ is the homogeneous strain, $\delta\varepsilon^c_{ij}(\mathbf{r})$ is the heterogeneous strain, $\varepsilon^0_{ij}(\mathbf{r})$ is the eigen strain in the γ phase, and V is the volume of the computational area (Eshelby, 1957). The homogeneous strain $\bar{\varepsilon}^c_{ij}$ is a uniform macroscopic strain. Assuming the free surface, $\bar{\varepsilon}^c_{ij}$ satisfies

$$\frac{\partial G_{str}}{\partial \bar{\varepsilon}^c_{ij}} = 0. \tag{11}$$

Therefore, the homogeneous strain $\bar{\varepsilon}^c_{ij}$ is given by

$$\bar{\varepsilon}^c_{ij} = C^{-1}_{ijkl}\sigma^A_{ij} + \frac{1}{V}\int_V \varepsilon^0_{ij} dV. \tag{12}$$

The heterogeneous strain $\delta\varepsilon^c_{ij}(\mathbf{r})$ is defined as the deviation from a homogeneous strain (Yamanaka et al., 2010). The heterogeneous strain satisfies:

$$\int_V \delta\varepsilon^c_{ij} dV = 0. \tag{13}$$

In the elastic model (Koyama & Onodera, 2003; Yamanaka et al., 2008), the heterogeneous energy is calculated by

$$\delta\varepsilon^c_{ij} = \frac{1}{(2\pi)^3}\int_k \frac{1}{2}\{n_i\Omega_{mj}(\mathbf{n}) + n_j\Omega_{mi}(\mathbf{n})\}\hat{\sigma}^0_{mn}(\mathbf{k})n_n \exp(i\mathbf{kr})d\mathbf{k}, \tag{14}$$

where $\Omega_{ik}(\mathbf{n})$ is the Green function tensor inverse to $\Omega_{ik}(\mathbf{n})^{-1} = C_{ijkl}n_j n_l$. $\mathbf{k}$ denotes the reciprocal space vector. $\mathbf{n} = \mathbf{k}/|k|$ is the unit vector along the $\mathbf{k}$ direction. $\hat{\sigma}^0_{ij} = C_{ijkl}\hat{\varepsilon}^0_{ij}$ is the Fourier transform of $\sigma^0_{ij} = C_{ijkl}\varepsilon^0_{ij}$. The elastic equation of the system is solved by a fast Fourier transform with respect to the displacement field (Khachaturian, 1983; Koyama & Onodera, 2003; Yamanaka et al., 2008).

Assuming an elastoplastic material, $\varepsilon^0_{ij}(\mathbf{r})$ is defined as the sum of the transformation-induced eigen strain $\varepsilon^t_{ij}(\mathbf{r})$ and plastic strain $\varepsilon^{p\prime}_{ij}(\mathbf{r})$ as (Guo et al., 2005),

$$\varepsilon^0_{ij}(\mathbf{r}) = \varepsilon^t_{ij}(\mathbf{r}) + \varepsilon^{p\prime}_{ij}(\mathbf{r}). \tag{15}$$

We assume that $\varepsilon^t_{ij}(\mathbf{r})$ is proportional to the phase-field parameter $\phi_q(\mathbf{r}, t)$ and calculated by

$$\varepsilon^t_{ij}(\mathbf{r}, t) = \sum_{p=1}^{N_\alpha}\sum_{q=N_\alpha+1}^{N} R_{ik}(\theta')R_{jl}(\theta')\varepsilon^{00}_{kl}(p, q)\phi_q(\mathbf{r}, t), \tag{16}$$

where $R_{ij}(\theta')$ is the rotation matrix which converts the local coordinate ("intra-crystalline coordinate system") system into the global coordinate system ("aggregate coordinate system") and $\varepsilon^{00}_{kl}(p, q)$ is the misfit strain between p and q in the local coordinate system of γ phase (Wang & Khachaturyan, 1997).

The evolution of plastic strain, $\varepsilon_{ij}^{p\prime}(\mathbf{r})$ is calculated as the sum of a term governed by the shear strain energy and creep strain when the differential stress $\Delta\sigma$ reaches a certain flow stress σ_F (Tsukada et al., 2011):

$$\varepsilon_{ij}^{p\prime}(\mathbf{r}) = \begin{cases} \varepsilon_{ij}^{p}(\mathbf{r}) & (\Delta\sigma < \sigma_F) \\ \varepsilon_{ij}^{p}(\mathbf{r}) + \varepsilon^{cp}(\mathbf{r}). & (\Delta\sigma \geq \sigma_F) \end{cases} \tag{17}$$

$\varepsilon_{ij}^{p}(\mathbf{r})$ is given by the following time-dependent Ginzburg-Landau (TDGL) equation (Guo et al., 2005):

$$\frac{\partial \varepsilon_{ij}^{p}}{\partial t} = -K_{ijkl}\frac{\delta G_{el}^{shear}}{\delta \varepsilon_{kl}^{p}}, \tag{18}$$

where K_{ijkl} is the fourth-order kinetic coefficient tensor for the plastic strain, and δ is the functional derivative. Considering the relationship of the subscripts, K_{ijkl} is linear and given by $K_{ijkl} = (KC_{ijkl})^{-1}$ with constant K. G_{el}^{shear} is the shear strain energy (Guo et al., 2005), which is calculated as

$$G_{el}^{shear} = \frac{1}{2}\int_V C_{ijkl}(e_{ij}^{c} - e_{ij}^{0})(e_{kl}^{c} - e_{kl}^{0})dV, \tag{19}$$

where e_{ij}^{c} and e_{ij}^{0} are the deviatoric components of the total strain and total eigen strain tensors, respectively. This study assumes that plastic deformation occurs when the shear strain energy reaches a certain value determined by the yield stresse σ_Y.

The evolution of creep strain, $\varepsilon_{ij}^{cp}(\mathbf{r})$ is experimentally calculated by

$$\dot{\varepsilon}^{cp} = A\sigma^{n}\exp\left(-\frac{Q}{RT}\right) \tag{20}$$

where A is a constant, σ is the flow stress, n is the stress exponent, and Q is the activation energy (e.g., Kirby, 1983).

To test the numerical implementation, we investigated the case of a single spherical particle. The details of the procedure and results are shown in the supplementary file.

3 Parameter setting

3.1 Experimental conditions

The governing equations in Eqs. (1) and (18) were solved using the finite-difference method, as in previous studies (Takaki et al., 2009, 2014). We used a finite-difference domain with 512×512 square meshes. When the length of one side of the mesh was set to Δl, the length of the model area L was $512 \times \Delta l$. For computational efficiency, we

Table 1. Experimental Parameters

Time increment Δt	0.004 s
Grain boundary thickness δ	$5 \times \Delta l^a$
Molar volume V	4.58×10^{-5} m^3/mol
Crystal lattice of α phase	$a = 4.908$ Å, $b = 10.302$ Å, $c = 6.025$ Å
Crystal lattice of γ phase	$a = b = c = 8.254$ Å
Yield stress at 1000 K	1200 MPa
Yield stress at 1200 K	500 MPa
Gap of entropy ΔS_e	-13.3 ± 0.6 [J $\cdot$ mol^{-1} $\cdot$ K^{-1}]
Heat capacity of α phase $(C_p)_\alpha$	$183.80 + 5.79 \times 10^3 \times T - 56.44 \times 10^{-5} \times T^{-\frac{1}{2}}$ [J $\cdot$ mol^{-1} $\cdot$ K^{-1}]
Heat capacity of γ phase $(C_p)_\alpha$	$156.11 + 30.50 \times 10^3 \times T - 36.50 \times 10^{-5} \times T^{-\frac{1}{2}}$ [J $\cdot$ mol^{-1} $\cdot$ K^{-1}]

[a] Δl: length of one side of a mesh.

introduce the algorithm proposed by Kim et al. (2006). The time increment was 0.004 s.

In Eqs. (2), (3), and (4), the grain boundary thickness is $\delta = 5 \times \Delta l$ (Takaki et al., 2014). Although the grain boundary energy γ_0 is proportional to the misorientation angle (Read & Shockley, 1950), for simplicity, we set several different constant values $\gamma_0 =$ 0.5, 1.0, 1.4 J/m^2 independent of the misorientation angle. These values are within the range of the grain boundary energy of the silicate olivine, $0.0 \leq \gamma_0 \leq 1.4$ J/m^2 (Duyster & Stöckhert, 2001). In Eq. (5), $V_m = 4.58 \times 10^{-5}$ m^3/mol was calculated using the Avogadro constant 6.02×10^{23} mol^{-1}, crystal lattices of α phase: $a = 4.908$ Å, $b =$ 10.302 Å, $c = 6.025$ Å, and the unit cell number of atoms of germanate olivine, 4 (Roy & Roy, 1954). In Eqs. (7) and (8), E_0 is given by:

$$E_0 = \Delta S_e \Delta T - \frac{\Delta C_{p,\ e}}{2T_e} \Delta T^2, \tag{21}$$

where ΔS_e is the entropy gap for the α–γ phase transformation, ΔT is the degree of supercooling, T_e is the temperature of the $\alpha - \gamma$ phase transformation, and $\Delta C_{p,\ e}$ is the gap in the heat capacity of the α and γ phases (Kashchiev, 2000):

$$\Delta C_{p,\ e} = (C_p)_\gamma - (C_p)_\alpha. \tag{22}$$

According to Ross and Navrotsky (1987), $\Delta S_e = -13.3 \pm 0.6$ [J $\cdot$ mol^{-1} $\cdot$ K^{-1}], $(C_p)_\alpha =$ $183.80 + 5.786 \times 10^3 \times T - 56.442 \times 10^{-5} \times T^{-\frac{1}{2}}$ [J $\cdot$ mol^{-1} $\cdot$ K^{-1}] and $(C_p)_\gamma = 156.11 +$

$30.50 \times 10^3 \times T - 36.498 \times 10^{-5} \times T^{-\frac{1}{2}}$ [J · mol^{-1} · K^{-1}]. In Eqs. (10) and (19), under the assumption of an isotropic elastic material, we adopted the elastic moduli of the germanate α phase ($K = 125$ GPa, $\mu = 72$ GPa, and $\nu = 0.259$, Liebermann, 1975). For simplicity, we set the elastic moduli of the γ phase to the same value as the α phase. In Eqs. (25) and (26), we used the crystal lattices of $X_\alpha = c = 6.025$ Å and $Y_\alpha = b = 10.302$ Å as the α phase (Roy & Roy, 1954), $X_\gamma = Y_\gamma = a = b = c = 8.254$ Å as the γ phase (Von Dreele et al., 1977). The yield stress of the aggregates was estimated from the results of Burnley et al. (1991). We set 1200 MPa and 500 MPa as the yield stresses of the aggregates at 1000 K and 1200 K, respectively. The flow stress of the α and γ phases, σ_F, is calculated using the following flow laws (Shi et al., 2015).

$$\alpha \text{ phase} : \dot{\varepsilon} = 10^{5.01} \sigma_F^{3.1} \exp\left(-\frac{441}{RT}\right), \tag{23}$$

$$\gamma \text{ phase} : \dot{\varepsilon} = 10^{-3.4} \sigma_F^{2.9} \exp\left(-\frac{228}{RT}\right). \tag{24}$$

After the differential stress reached the flow stress, we set $\dot{\varepsilon}_{11}^{cp} = 2.0 \times 10^{-4}$ s^{-1}. To calculate the misfit strain in Eqs. (16), $\varepsilon_{ij}^{00}(p, q)$, we must convert the local coordinate system to the global coordinate system (Figure 1(a)). First, the coordinate system of the p-th crystal lattice parameters of the α phase $L'_\alpha(p)$ are converted into the local coordinate system of the γ phase as follows:

$$L'_\alpha(p) = r(\theta - \theta') \begin{pmatrix} X_\alpha \\ Y_\alpha \end{pmatrix} = \begin{pmatrix} X'_\alpha \\ Y'_\alpha \end{pmatrix}, \tag{25}$$

where $r(\theta - \theta')$ is the rotation matrix, and X_α and Y_α are the crystal lattices of the α phase. The q-th crystal lattice parameters of the γ phase $L'_\gamma(q)$ are given by:

$$L_\gamma(q) = \begin{pmatrix} X_\gamma \\ Y_\gamma \end{pmatrix}, \tag{26}$$

where X_γ and Y_γ are the crystal lattices of the γ phase. Therefore, the misfit strain in Eq. (16), $\varepsilon_{ij}^{00}(p, q)$ is calculated as follows:

$$\varepsilon_{ij}^{00}(p, q) = \begin{pmatrix} \frac{X_\gamma(q) - X'_\alpha(p)}{X'_\alpha(p)} \\ \frac{Y_\gamma(q) - Y'_\alpha(p)}{Y'_\alpha(p)} \end{pmatrix}. \tag{27}$$

The kinetic parameter of Eq. (18) for the plastic strain is set to $K = 90$ as the stress-strain curves are closer to those of the previous study (Burnley et al., 1991). D in Eq. (5) is the diffusivity of Ge in germanate olivine, but it is unknown. Hence, we assumed D in Section 4.1 by comparing our results with those of previous experiments by Burnley et al. (1991). The details of the experimental parameters are listed in Table 1.

Table 2. Experimental Parameters and results

Run	P^a [GPa]	T^b [K]	$\dot{\varepsilon}$ [s^{-1}]	L^c [μm]	γ_0 [J/m^2]	VL^d [%]
SP1T1	1.0	1000	-	60	1.4	0.079
SP3T1	3.0	1000	-	60	1.4	0.079
SP5T1	5.0	1000	-	60	1.4	0.079
SP1T1.2	1.0	1200	-	60	1.4	0.77
SP3T1.2	3.0	1200	-	60	1.4	0.12
SP5T1.2	5.0	1200	-	60	1.4	0.21
P1T1	1.0	1000	2.0×10^{-4}	60	1.4	0.079
P3T1	3.0	1000	2.0×10^{-4}	60	1.4	0.079
P5T1	5.0	1000	2.0×10^{-4}	60	1.4	0.079
P1T1.2	1.0	1200	2.0×10^{-4}	60	1.4	0.66
P3T1.2	3.0	1200	2.0×10^{-4}	60	1.4	2.02
P5T1.2	5.0	1200	2.0×10^{-4}	60	1.4	0.33
SP1T1.2NP^e	1.0	1200	-	60	1.4	0.082
SP5T1.2NP^e	5.0	1200	-	60	1.4	0.079
P1T1.2NP^e	1.0	1200	2.0×10^{-4}	60	1.4	0.079
P5T1.2NP^e	5.0	1200	2.0×10^{-4}	60	1.4	0.076
P1T1.2GB	1.0	1200	2.0×10^{-4}	60	1.0	0.67
P5T1.2GB	5.0	1200	2.0×10^{-4}	60	1.0	0.33
P1T1.2GB2	1.0	1200	2.0×10^{-4}	60	0.5	0.67
P5T1.2GB2	5.0	1200	2.0×10^{-4}	60	0.5	0.34

[a]Confining pressure. [b]Temperature. [c]Length of model area.

[d]Volume fraction of γ phase at $\varepsilon_1 = 9$ %. [e] without plastic and creep strains

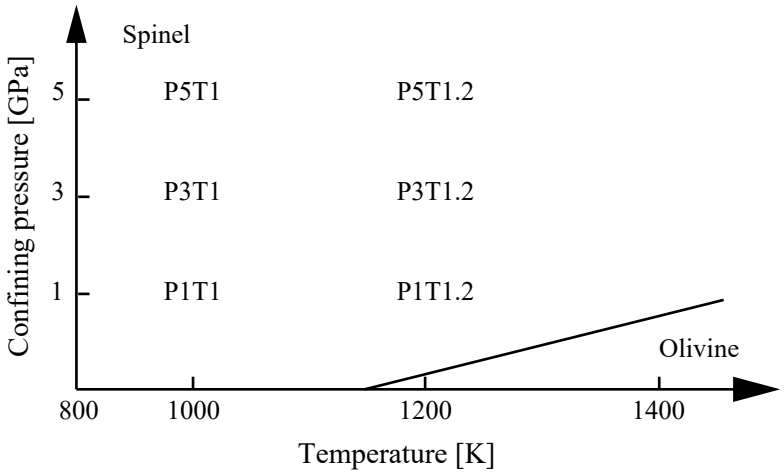

Figure 2. Phase diagram (after Ross & Navrotsky, 1987) and conditions of numerical experiments.

Under the above conditions, we conducted the following four simulations in which all α grains were metastable (Figure 2). (1) We conducted deformation simulations (Runs P1T1-P5T1.2) at different pressures and temperatures, as shown in Figure 2, to reveal the pressure and temperature dependence on the grain growth of the γ phase. Furthermore, to reveal the effect of deformation on the grain growth of the γ phase, we conducted both static (Runs SP1T1-SP5T1.2) and deformation simulations (Runs P1T1-P5T1.2). (2) To reveal the effect of plastic strain on the grain growth, we conducted simulations with plastic strain ($\varepsilon_{ij}^{p\prime}$) accompanied with the phase transformation in the static experiments (Runs SP1T1.2 and SP5T1.2), without plastic strain in the static experiments (Runs SP1T1.2NP and SP5T1.2NP), with plastic strain in the deformation experiments (Runs P1T1.2 and P5T1.2), and without plastic strain in the deformation experiments (Runs P1T1.2NP and P5T1.2NP). (3) To reveal the effect of grain boundary energy on the grain growth, we conducted simulations at three different values of the grain boundary energy: 1.4 J/m^2 (Runs P1T1.2 and P5T1.2), 1.0 J/m^2 (Runs P1T1.2GB and P5T1.2GB), and 0.5 J/m^2 (Runs P1T1.1GB2 and P5T1.2GB2). These conditions are listed in Table 2. All simulations were stopped after reaching an axial strain (ε_1) of 9 % (450 s), according to a previous study (Burnley et al., 1991).

4 Results

4.1 Evaluation of undetermined grain boundary mobility, M_0

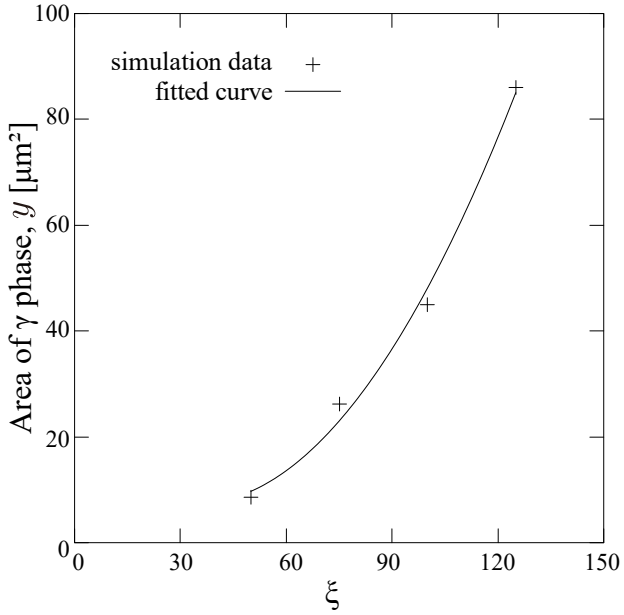

Figure 3. Area variation of γ phase with ξ. The solid line is a regression quadratic function: $y = 9.4427 \times 10^{-3}\xi^2 - 6.4926 \times 10^{-1}\xi + 1.8594 \times 10$. The coefficient of determination was $R^2 = 0.9998$.

Although the calculation of the grain boundary mobility M_0 in Eq. (5) requires the diffusivity of Ge in germanate olivine D, and D has not yet been experimentally determined. Hence, we numerically constrained D using the flow law of germanate olivine. The strain rate $\dot{\varepsilon}$ is theoretically given by the following flow law of dislocation creep:

$$\dot{\varepsilon} = \frac{Db\sigma^3}{kG^2}, \tag{28}$$

where D is the lattice diffusivity, b is the Burgers vector, σ is the strength, k is the Boltzmann constant, and G is the shear modulus (Meyers et al., 1999). In the flow law of germanate olivine, only dislocation creep was experimentally determined and is given by Eq. (23). Given that the theoretical flow law (Eq. (28)) and the experimentally determined flow law (Eq. 20) are identical, we can acquire the following equation:

$$\begin{aligned} D &= \left(\frac{\sigma^n}{\sigma^3}\right)\frac{kG^2A}{b}\exp\left(-\frac{Q}{RT}\right) \\ &= \xi\frac{kG^2A}{b}\exp\left(-\frac{Q}{RT}\right). \end{aligned} \tag{29}$$

We set $\xi = (\sigma^n/\sigma^3)$, $k = 1.38 \times 10^{-23}$ J/K. $G = 70.3$ GPa (Weidner & Hamaya, 1983). According to Shi et al. (2015), $A = 10^{5.01}$ MPa$^{\mathrm{n}}$s^{-1}, $Q = 441$ kJ/mol. The Burgers vector b is 0.4915 nm (Dupas-Bruzek et al., 1998). To determine the diffusivity of Ge in germanate olivine D, we must calculate the undetermined constant ξ in Eq. (29), which depends on the strength σ and the stress exponent n.

Thus, we conducted numerical simulations with several different values $\xi = 50$, 75, 100, 125 under identical conditions to the deformation experiment GL299 (Burnley et al., 1991; Burnley, 1995), and calculated the grain area of the γ phase. By comparing the grain area of the γ phase in this simulation with that calculated from the result of the deformation experiment GL299 (Burnley et al., 1991; Burnley, 1995), we determined the reasonable ξ. The numerical simulations were conducted at a pressure of 1.19 GPa, temperature of 1210 K, strain rate of 2.0×10^{-4} s^{-1}, experimental duration of 450 s, $L = 60$ μm, and $\gamma_0 = 1.4$ J/m, which are identical to GL299 (Burnley et al., 1991; Burnley, 1995). Three grains of the γ phase were introduced in advance. The other experimental conditions are listed in Table 2. We also stopped the simulation at $\varepsilon_1 = 9$ % (450 s) because the maximum axial strain (ε_1) in GL299 was 9 % (Burnley et al., 1991; Burnley, 1995).

The results are shown in Figure 3. We fitted the grain area variation of the γ phase to the following quadratic function:

$$y = 9.4427 \times 10^{-3}\xi^2 - 6.4926 \times 10^{-1}\xi + 1.8594 \times 10, \tag{30}$$

where y is the area of the γ phase grown from the initial three grains of the γ phase, and the coefficient of determination is $R^2 = 0.9998$ (solid line in Figure 3).

We calculated the grain area of the γ phase in GL299 (Burnley et al., 1991) from a growth rate of 4.37×10^{-9} m/s. When we hypothesize that the grain is spherical, the increment of the grain radius is 1.97 μm at growth rates of 4.37×10^{-9} m/s and an experimental duration of 450 s. Because we introduced three grains of the γ phase in advance in the numerical simulation, we also hypothesized that the number of initial grains of the γ phase was 3 when we calculated the grain area of the γ phase in GL299 (Burnley et al., 1991). Consequently, the grain area of the γ phase in GL299 was 36.4 μm^2 after the experiment.

Substituting 36.4 μm^2 into Eq. (30), we obtain $\xi = 89.8$. Using this value, we can obtain the stress exponent $n = 3.2$ from $\xi = (\sigma^n/\sigma^3)$, where $\xi = 89.8$ and experimentally obtained flow stress of $\sigma = 1224$ MPa (Burnley, 1990). The stress exponent (approximately 3.2) estimated from the calculation is consistent with the stress exponent of the Mg_2GeO_4 spinel harzburgite of 2.9±1.0 reported experimentally by Shi et al. (2015).

4.2 Volume fraction of γ phase

Table 2 shows the calculated volume fraction VL of γ phase after 450 s. γ phase does not grow at 1000 K in either static (Runs SP1T1-SP5T1) or deformation (Runs P1T1-P5T1) simulations. At 1200 K, the γ phase grows in both static (Runs SP1T1.2-SP5T1.2) and deformation (Runs P1T1.2-P5T1.2) simulations. In the static simulations at 1200 K (Runs SP1T1.2-SP5T1.2), the volume fraction of γ increases as confining pressures increase from 1 GPa to 5 GPa. In the deformation simulations at 1200 K (Runs P1T1.2-P5T1.2), the volume fraction of γ increases as confining pressures increase from 1 GPa to 3 GPa, whereas the volume fraction decreases as confining pressures increase from 3 GPa to 5 GPa. The volume fraction of γ phase in deformation simulations (Runs P1T1.2-P5T1.2) is larger than that in static simulations (Runs SP1T1.2-SP5T1.2), respectively. This is also shown in Figure 4. The effect of plastic strain on the volume fraction of γ phase is shown in Table 2. The plastic strain is generated by the deformation and the eigen strain associated with the phase transformation. The volume fraction of the γ phase does not increase in static and deformation experiments without plastic strain. Although the grain boundary energy changes from 0.5 J/m^2 (Runs P1T1.2GB2 and P5T1.2GB2) to 1.4 J/m^2 (Runs P1T1.2 and P5T1.2), the volume fraction of γ phase does not change.

4.3 Microstructure

The microstructural development of the $\alpha-\gamma$ aggregates with plastic strain at 1 and 3 GPa and 1200 K is shown in Figures 5 and 6, respectively. γ grains grew around the initial γ grains and along the grain boundaries. In particular, lens-shaped γ grains grow perpendicular to the axial stress in the deformation simulations (black arrows in Figures 5 and 6). The von Mises stress increases around the grains of the γ phase and inside some of the α phases (Figures 5b and 6b). The shear component of plastic strain (called shear plastic strain, $\varepsilon_{12}^{p\prime}$) increases around γ grains and inside of α grains in the

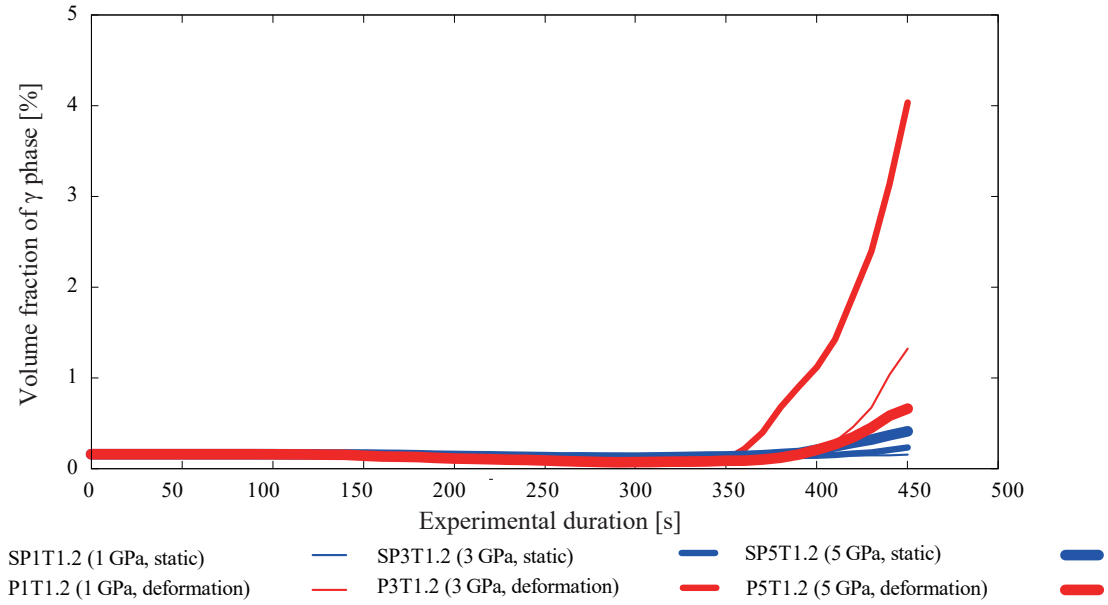

Figure 4. Volume fraction of γ phase as a function of the experimental duration with plastic strain. (a) SP1T1.2: static simulation at $P = 1$ GPa and $T = 1200$ K. P1T1.2: deformation simulation at $P = 1$ GPa and $T = 1200$ K. SP3T1.2: static simulation at $P = 3$ GPa and $T = 1200$ K. P3T1.2: deformation simulation at $P = 3$ GPa and $T = 1200$ K. SP5T1.2: static simulation at $P = 5$ GPa and $T = 1200$ K. P5T1.2: deformation simulation at $P = 5$ GPa and $T = 1200$ K.

deformation simulations (Figures 5c and 6c). In deformation simulations, the shear plastic strain developed sub-horizontally (almost perpendicular to the maximum compression direction). Therefore, in Figures 5 and 6, the eigen strain also develops sub-horizontally because of Eq. (15). The microstructural development of the $\alpha-\gamma$ aggregates with plastic strain at 5 GPa and 1200 K is shown in Figure 7. The grains of the γ phase are rounded in the static simulations (shown by the black arrows in Figures 7a). The grains of the γ phase are elongated like an ultra-thin tail in the deformation simulations (shown by an orange arrow in Figure 7c). The horizontal evolution of the shear plastic strain in the static simulations was weaker than that in the deformation simulations (Figures 7b and d).

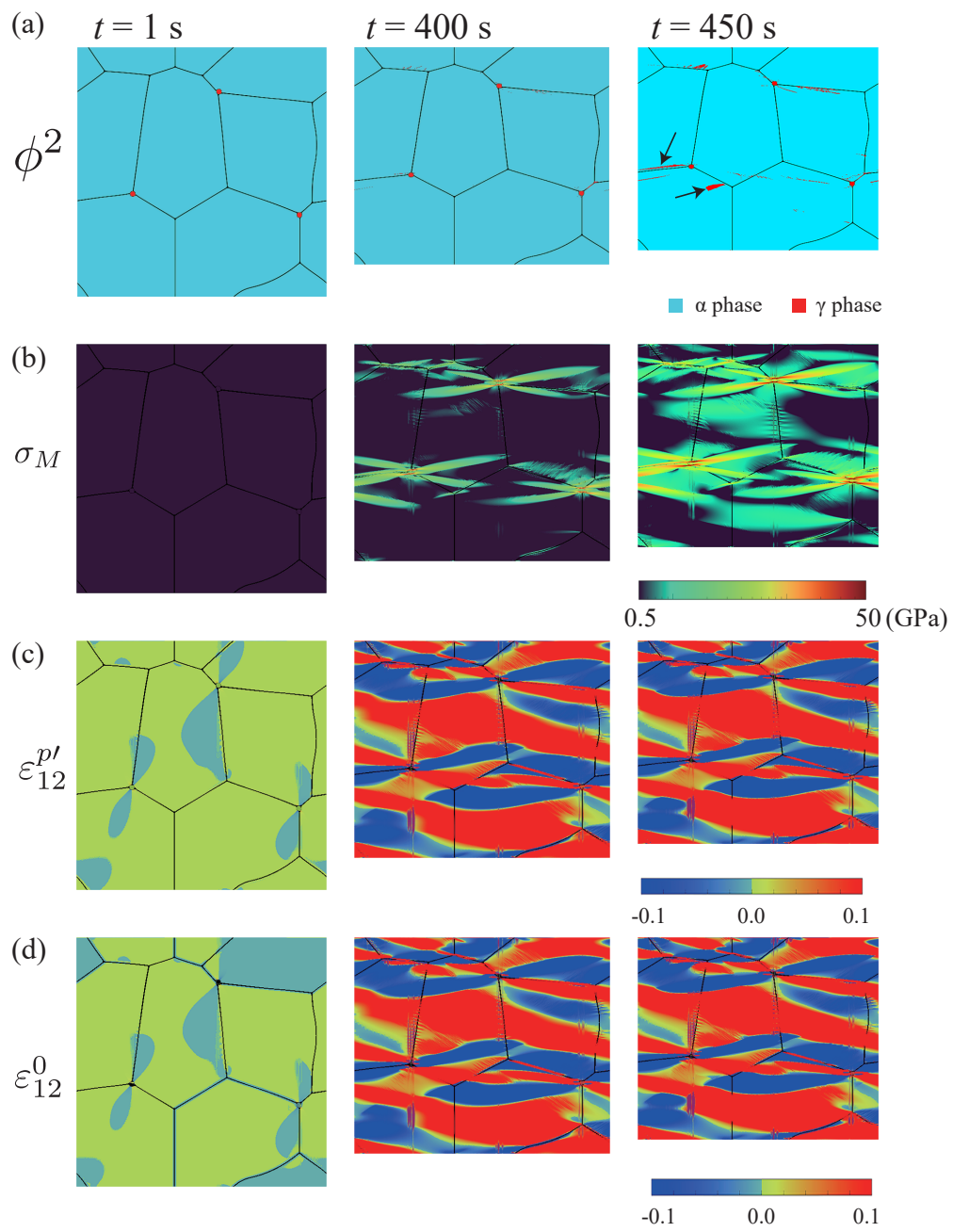

Figure 5. Microstructure development of $\alpha \rightarrow \gamma$ aggregates in the deformation simulations at $P = 1$ GPa and $T = 1200$ K (Run P1T1.2). (a) Grain growth of the γ phase as the experimental duration increases. Only the γ phase with $\phi \geq 0.8$ is visualized. The phase-field parameter ϕ was multiplied to visualize the grain boundaries. The black arrow shows the lens-shaped grains of the γ phase. (b) Von Mises stress evolution. (c) Shear plastic strain evolution (d) Shear eigen strain evolution. Animations are shown in Videos S1-S4.

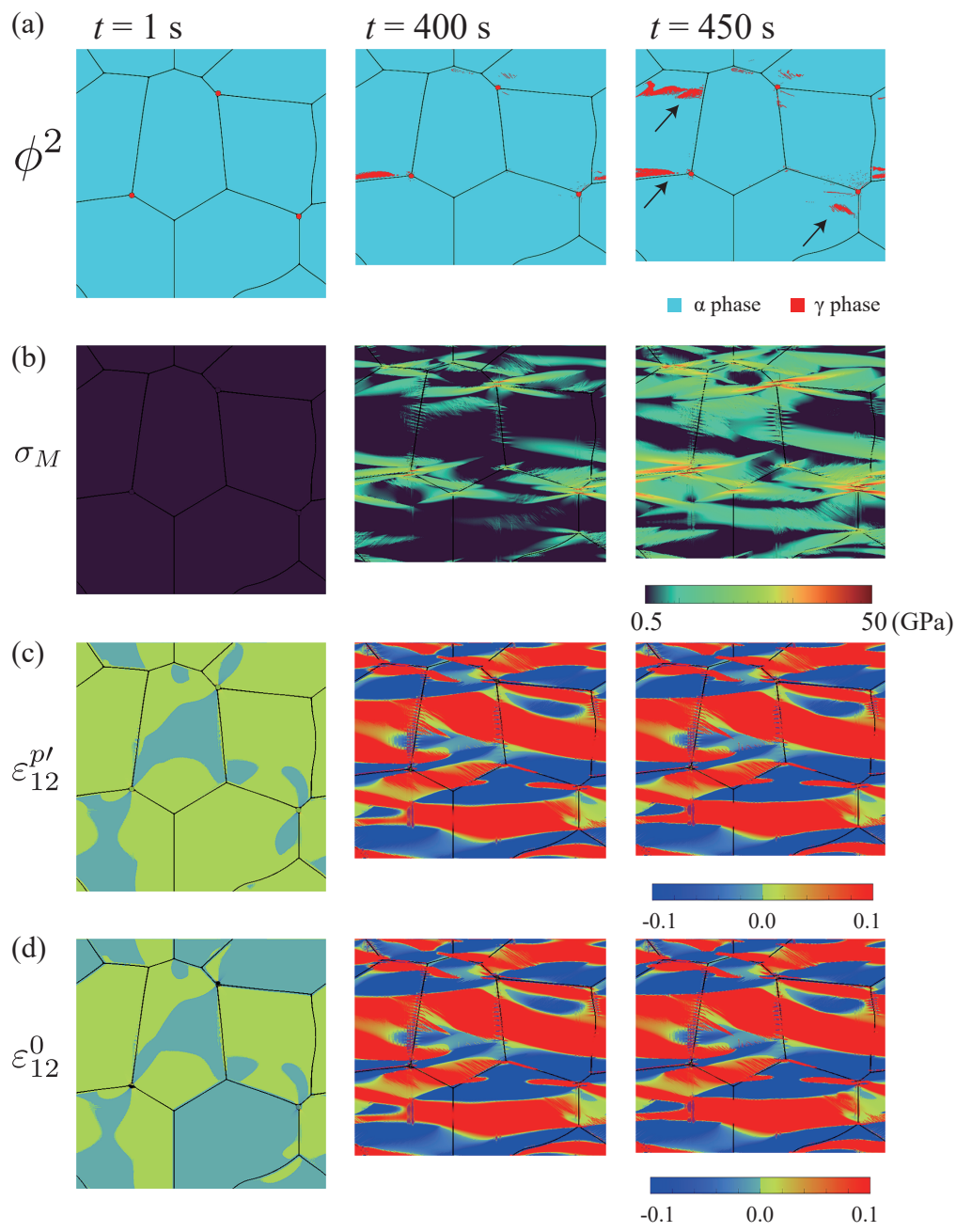

Figure 6. Microstructure development of $\alpha \rightarrow \gamma$ aggregates in the deformation simulations at $P = 3$ GPa and $T = 1200$ K (Run P3T1.2). (a) Grain growth of the γ phase as the experimental duration increases. Only the γ phase with $\phi \geq 0.8$ is visualized. The phase-field parameter ϕ was multiplied to visualize the grain boundaries. Black arrows show the lens-shaped grains of the γ phase. (b) Von Mises stress evolution. (c) Shear plastic strain evolution. (d) Shear eigen strain evolution. Animations are shown in Videos S5-S8.

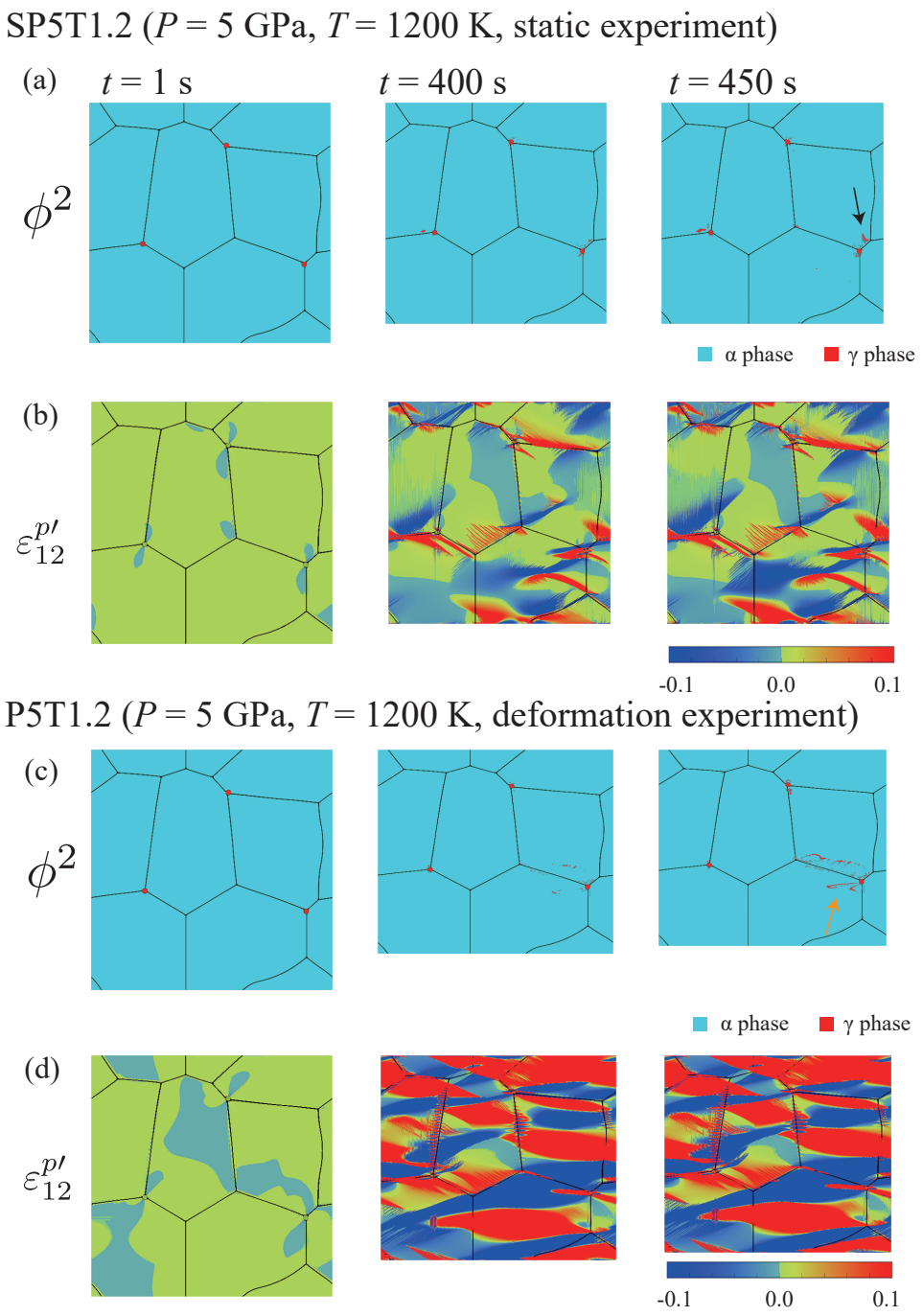

Figure 7. Microstructure development of $\alpha \rightarrow \gamma$ aggregates in both static (a, b) and deformation (c, d) simulations at $P = 5$ GPa and $T = 1200$ K (Runs SP5T1.2 and P5T1.2). (a, c) Grain growth of the γ phase as the experimental duration increases. Only the γ phase with $\phi \geq 0.8$ is visualized. The phase-field parameter ϕ was multiplied to visualize the grain boundaries. Black arrows show rounded grains of γ phase. The orange arrow shows the γ grains like a tail. (b, d) Shear plastic strain evolution. Animations are shown in Videos S9-S12.

5 Discussion

5.1 Effect of deformation, overpressure, grain boundary, and plastic strain

As Table 2 and Figure 4 show, the volume fraction of the γ phase under differential stress (Runs P1T1.2-P5T1.2) is larger than that under static conditions (Runs SP1T1.2-SP5T1.2). Generally, the elastic strain energy around the γ phase (precipitated phase) inhibits the grain growth of the γ phase (e.g., Liu et al., 1998; Steinbach & Apel, 2006). Thus, the volume fraction of the γ phase decreases as the elastic strain energy increases. The elastic strain energy under differential stress is larger than that under static conditions because of the deformation; therefore, the grain growth of the γ phase is inhibited under differential stress. Nevertheless, in this simulation, the opposite results were obtained. This was caused by the shear plastic strain. Figure 8 shows the plastic strains ($\varepsilon_{11}^{p\prime}$, $\varepsilon_{22}^{p\prime}$, and $\varepsilon_{12}^{p\prime}$) distributions of the modeled area with 512×512 square meshes in both simulations at 1200 K with plastic strain. The plastic strains ($\varepsilon_{11}^{p\prime}$, $\varepsilon_{22}^{p\prime}$, and $\varepsilon_{12}^{p\prime}$) distributions under the deformation conditions are different from those under static conditions. Compressive (positive) plastic strains ($\varepsilon_{11}^{p\prime}$ and $\varepsilon_{22}^{p\prime}$) governed by the shear elastic strain energy (Eqs. (18) and (19)) are generated by compressive stress, whereas the extension (negative) plastic strain ($\varepsilon_{11}^{p\prime}$ and $\varepsilon_{22}^{p\prime}$) is generated by the transformation-induced eigen strain derived from the negative volume change of the $\alpha \rightarrow \gamma$ phase transformation. The shear plastic strain ($\varepsilon_{12}^{p\prime}$) was also generated by the transformation-induced eigen strain. As the extension plastic strain increases with the grain growth of the γ phase, it locally reduces the elastic strain energy, and the volume fraction of the γ phase further increases. The reduction in the elastic energy associated with plastic strain due to a phase transformation is also known in metals (Yamanaka et al., 2010; Ammar et al., 2011). However, the compressive plastic strain ($\varepsilon_{11}^{p\prime}$ and $\varepsilon_{22}^{p\prime}$) dominate over the extension strain derived from the transformation-induced eigen strain under the deformation conditions (Figures 8(j), (k), (m), (n), (p), and (q)). Therefore, $\varepsilon_{11}^{p\prime}$ and $\varepsilon_{22}^{p\prime}$ do not promote the grain growth of the γ phase in the $\alpha \rightarrow \gamma$ phase transformation. Meanwhile, the shear plastic strain distribution under differential conditions (Figures 8(l), (o), and (r)) is different from that under static conditions (Figures 8(c), (f), and (i)). Furthermore, the average magnitude of the shear plastic strain in the differential conditions was larger than that in the static conditions. The shear plastic strain promotes the grain growth of the γ phase in the $\alpha \rightarrow \gamma$ phase transformation. Without plastic strain, the volume

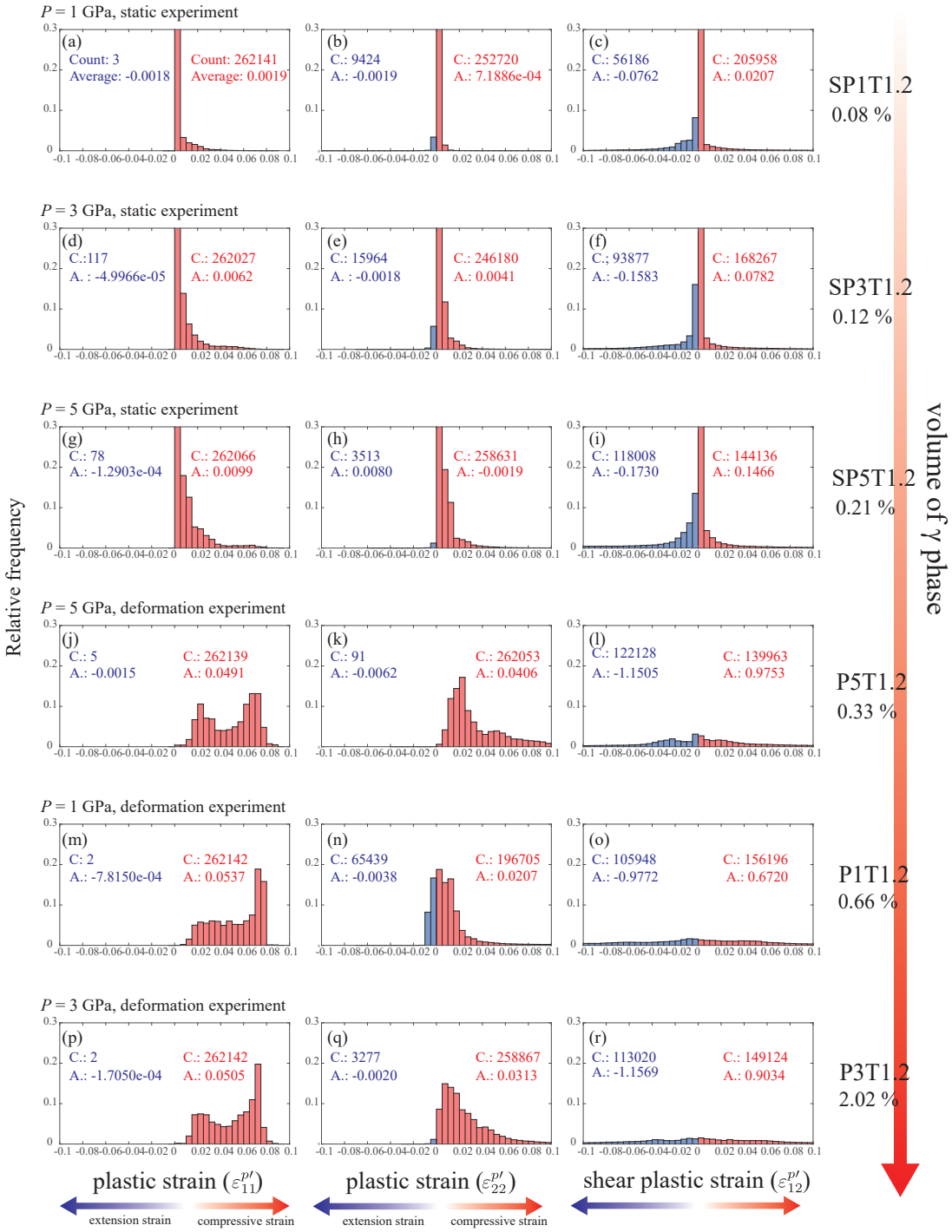

Figure 8. Effect of plastic strain on the volume fraction of γ phase in both simulations at 1200 K with plastic strain. The plastic strain ($\varepsilon_{11}^{p\prime}$, $\varepsilon_{22}^{p\prime}$, and $\varepsilon_{12}^{p\prime}$) distribution of the modeled area with 512 $\times$ 512 square meshes and the volume fraction of the γ phase (right next to the plastic strain distribution). The red and blue bins represent positive and negative plastic strains, respectively. The blue "Count (C)" shows the sum of the absolute frequencies of the negative strain. The blue "Average (A)" shows the average magnitude of the negative strain. In contrast, the red "Count (C)" shows the sum of the absolute frequencies of the positive strains. The blue "Average (A)" shows the average magnitude of the positive strain.

fraction of the γ phase does not increase (Table 2 and Figure 4). This also indicates that plastic strain is essential for the grain growth of the γ phase.

As the confining pressure increased, the elastic strain energy that inhibited the grain growth of the γ phase increased. At the same time, the chemical-free energy promoting the grain growth of the γ phase also increases because of the large overpressure. Hence, the volume fraction of the γ phase is determined by the competition between the chemical energy that promotes grain growth and the elastic strain energy inhibiting grain growth. As a result, as the confining pressure increased, the volume fraction of the γ phase decreased or increased depending on the magnitudes of the elastic strain energy and the chemical-free energy. As Table 2 and Figure 4 show, under the deformation conditions, the volume fraction of the γ phase at 3 GPa is larger than that at 1 and 5 GPa. This indicates that the chemical-free energy dominates over the elastic free energy at less than 3 GPa, whereas the elastic strain energy dominates the chemical free energy at more than 3 GPa. Meanwhile, under static conditions, the volume fraction of the γ phase increases as the confining pressure increases. This indicates that the chemical-free energy dominates the elastic strain energy over a wide range of confining pressures.

As Eqs. (1) and (3) show that the grain boundary energy is related to the gradient energy that promotes the grain growth of the γ phase: a large grain boundary energy indicates large gradient energy. Nevertheless, the volume fraction of the γ phase did not increase with the grain boundary energy. This indicates that the gradient energy is smaller than the elastic strain energy and chemical energy, and it hardly affects the grain growth of the γ phase under these conditions. Therefore, we can assume that the volume fraction of the γ phase is independent of the misorientation angle of the α phase.

Most of the γ phase is lens-shaped under differential stress at low pressure with plastic strain (Figures 5a and 6a). Meanwhile, most of the γ phase is ultra-thin under differential stress at high pressure (Figure 7c). This difference was caused by the elastic strain energy. The stable shape of the precipitated phase, such as the γ phase, is determined by the balance between the elastic strain energy and the gradient energy (Nabarro, 1940). When the elastic strain energy and the volume of the precipitated phase are large, the stable shape becomes thin, which can reduce the elastic strain energy, as revealed by the calculation of the elastic strain energy of the precipitated phase using the axial ratio of

its geometry as a variable (e.g., Pineau, 1976; Miyazaki et al., 1979). Therefore, under differential stress, the γ grains become thin. Furthermore, as the confining pressure increases, the elastic strain energy increases; thus, the thickness of the γ grains becomes even thinner. The horizontal elongation of γ grains is caused by the evolution of the shear plastic strain in the horizontal direction. Under static conditions, γ grains are rounded, and the shear plastic strain does not develop strongly in the horizontal direction (Figures 7a and b). Meanwhile, under differential stress, most of the γ grains are perpendicular to the maximum compressive direction, and the shear plastic strain develops strongly in the horizontal direction. In other words, the elastic strain energy and shear plastic strain would control the shape of the γ grains.

The distribution of shear plastic strain developing sharply in the horizontal direction (perpendicular to the maximum compression direction) is similar to that of shear stress by wedge disclination (e.g., Fig. 2a Capolungo & Taupin, 2019). A pair of positive and negative shear plastic strains developed horizontally with γ grains at the core (e.g., in Run P3T1.2, Supplementary figure S2). Disclinations are line defects characterized by a rotational misfit (e.g., Volterra, 1907; Hirth et al., 2020). The eigen strain generating plastic strain has shear components owing to Eq. (16). Although the boundary conditions assume that boundaries are not constrained, the eigen strain that cannot be resolved on the boundaries would generate the disclination derived from the rotational misfit.

5.2 Comparison with previous study and the implication for metastable olivine wedge

Many previous studies conducted deformation experiments of metastable germanate olivine (α phase) under conditions ($P = 1-5$ GPa, $T = 900-1500$ K), similar to our numerical conditions (e.g., Green et al., 1990; Burnley et al., 1991; Tingle et al., 1993; Schubnel et al., 2013; Wang et al., 2017; Sawa, Muto, et al., 2021; Sawa, Miyajima, et al., 2021). The partial $\alpha \rightarrow \gamma$ phase transformation resulted in faulting with a large stress drop and acoustic emissions (AEs) called transformational faulting (e.g., Tingle et al., 1993; Schubnel et al., 2013; Wang et al., 2017). Faulting occurred at a limited window of temperatures (approximately 1100-1300 K at 1 GPa), where the α and γ phases could coexist. At lower temperature than the window (<1100 K), the samples behaved ductile with differential stress > 2.0 GPa (called strong ductile in Burnley et al., 1991) be-

cause α phase did not undergo the phase transformation to γ phase. At a higher temperature than the window (<1400 K), the samples behaved ductile with differential stress > 0.5 GPa (called weak ductile) because α phase completely underwent the phase transformation to γ phase. In our simulations, we set the temperature dependence on the grain boundary mobility M_{ij} as Eqs. (5) and (29), respectively. Therefore, we reproduce a similar temperature dependence of the $\alpha \rightarrow \gamma$ phase transformation such that the γ phase did not grow at 1000 K but at 1200 K (Table 2). However, we did not set the temperature dependence of the plastic strain in Eq. (15) and (19), respectively. Therefore, it was not easy to reproduce the mechanical behavior during phase transformation fully in this study. The experiments conducted at high confining pressures of 2-5 GPa reported that faulting occurred on the nano-shear bands of fine-grained γ grains (Schubnel et al., 2013; Wang et al., 2017). On the other hand, the experiments conducted at a low confining pressure of 1-2 GPa reported that faulting occurred at lens-shaped anticracks composed of fine-grained γ phase with a strong preferred orientation normal to the maximum compression direction (Green & Burnley, 1989; Burnley et al., 1991). As discussed above, under differential stress at a low confining pressure, shear plastic strain develops sharply in the horizontal direction (normal to the maximum compression direction). Furthermore, when the elastic strain energy and volume of the γ phase are large, the stable shape becomes thin. Therefore, lens-shaped γ grains grow with a strong preferred orientation normal to the maximum compression direction in the simulation. Although the anticracks in the previous study are composed of fine-grained γ grains, and we did not simulate the nucleation, if the anticrack can be considered as a single crystal, these lens-shaped γ grains are similar to anticracks reported by previous deformation experiments at a low confining pressure (Green & Burnley, 1989; Burnley et al., 1991). Under differential stress at a high confining pressure, the elastic strain energy is large; therefore, the grain shapes of the γ phase become even thinner. These ultra-thin γ grains are similar to the nano-shear bands reported in previous deformation experiments at a high confining pressure (Schubnel et al., 2013; Wang et al., 2017). Nano shear bands are composed of nanocrystalline spinel nucleated along the (010) and (110) dislocations in the host α grains (Riggs & Green, 2005). Although we did not simulate the nucleation, the formation of the ultra-thin γ grains means that the thin forms are stable for the energy under high confining pressure, and this would be applicable even in the nucleation along the dislocation forming nano shear bands.

According to Mosenfelder et al. (2001), when the intracrystalline transformation of β and γ phases is considered, the depth of metastability of olivine is reduced by as much as 100 km, owing to the large increase in the density of nucleation sites for the intracrystalline nucleation at the deep part of the subducting slabs with a large overpressure. Inhibition of growth by transformational stress can increase the depth interval over which the phase transformation takes place, but this is unlikely to be a dominant factor if intracrystalline transformation occurs (Mosenfelder et al., 2001). This previous model was based on the results of static experiments considering only the eigen strain owing to the phase transformation in the static condition and did not consider the effect of deformation in the subducting slab. As discussed above, the deformation increases the elastic strain energy, inhibiting the grain growth of the γ phase. However, the shear plastic strain promoting the grain growth of the γ phase under differential stress was larger than that under the static condition. This indicates that the γ grains under differential stress grow more easily than those under static conditions. However, at large overpressures, the elastic strain energy inhibiting grain growth and the chemical-free energy leading to grain growth increase simultaneously. At pressures larger than 3 GPa, considering our simulation results, the effect of the elastic strain energy on the grain growth is larger than that of the chemical-free energy. The transformation rate is determined by the combination of nucleation and grain growth, and this simulation does not consider nucleation. Nevertheless, at a slight overpressure, we assume that the depth of metastability of olivine is decreased more than that in a previous study that considered intracrystalline nucleation (Mosenfelder et al., 2001). Conversely, at a large overpressure, the depth of metastability of olivine increases. The deformation also increases the density of nucleation sites (e.g., Dupas-Bruzek et al., 1998). This indicates that phase transformation is promoted by an increase in the density of nucleation sites during deformation. Thus, we need to build a model that considers nucleation and grain growth to reveal the effect of the deformation on the phase transformation more accurately.

6 Conclusions

We simulated the growth of the germanate γ phase under various mechanical and microstructural conditions using the phase-field method to reveal the microstructural growth kinetics of the $\alpha \rightarrow \gamma$ phase transformation and the difference in the formation conditions between anticracks at a low confining pressure and narrow bands comprising

fine-grained γ grains at a high confining pressure. The volume fraction depends on the magnitude of the confining pressure due to the competition between the chemical-free energy promoting grain growth and the elastic strain energy inhibiting grain growth. Under static conditions, the chemical-free energy controls the grain growth of the γ phase over a wide range of pressures. Under differential stress, at a slight overpressure, the chemical-free energy controls the grain growth of the γ phase. Meanwhile, at large overpressures, the elastic strain energy controls the grain growth of the γ phase. Furthermore, the shear plastic strain promoting the grain growth of the γ phase develops under differential stress more vigorously than under static conditions and conditions without plastic strain. Therefore, the volume fraction of the γ phase under differential stress is larger than that under the other conditions. The grains of the γ phase under differential stress at low confining pressure (1 and 3 GPa) are lens-shaped with a strong preferred orientation normal to the maximum compression direction because the shear plastic strain accompanied by the phase transformation develops sharply in the horizontal direction, and the elastic strain energy and γ grains are large. These lens-shaped γ grains are similar to those observed in previous deformation experiments at low confining pressures ranging from 1 to 2 GPa (Green & Burnley, 1989; Burnley et al., 1991). Meanwhile, the grains of γ phase at a high confining pressure (5 GPa) are ultra-thin because the elastic strain inhibiting the grain growth is larger than that at low confining pressure These thin γ grains are similar to the nano-shear bands observed in previous deformation experiments at a high confining pressure of 5 GPa (Schubnel et al., 2013; Wang et al., 2017).

Open Research

The scripts for this simulation are available through Mendelay Data (https://data.mendeley.com/datasets/ztjkb9
09b4-4d21-a590-b7d870db11c1)

Acknowledgments

We would like to thank Julien Gasc, an anonymous reviewer, for their helpful suggestions for improving the manuscript. This work was supported by the International Joint Graduate Program in Earth and Environmental Sciences, Tohoku University, JSPS KAKENHI Grant Numbers JP20J12328, JP19H05117, JP21H00090, and the Ministry of Education, Culture, Sports, Science and Technology (MEXT) of Japan, under its Earthquake and Volcano Hazards Observation and Research Program.

References

Akaogi, M., Ito, E., & Navrotsky, A. (1989). Olivine-modified spinel-spinel transitions in the system Mg_2SiO_4-Fe_2SiO_4: Calorimetric measurements, thermochemical calculation, and geophysical application. *Journal of Geophysical Research: Solid Earth*, *94*(B11), 15671–15685. doi: 10.1029/JB094iB11p15671

Ammar, K., Appolaire, B., Cailletaud, G., & Forest, S. (2011). Phase field modeling of elasto-plastic deformation induced by diffusion controlled growth of a misfitting spherical precipitate. *Philosophical Magazine Letters*, *91*(3), 164–172. doi: 10.1080/09500839.2010.541891

Boland, J. N., & Liu, L.-g. (1983). Olivine to spinel transformation in Mg_2SiO_4 via faulted structures. *Nature*, *303*(5914), 233–235. doi: 10.1038/303233a0

Brearley, A. J., Rubie, D. C., & Ito, E. (1992). Mechanisms of the transformations between the α, β and γ polymorphs of Mg_2SiO_4 at 15 GPa. *Physics and Chemistry of Minerals*, *18*(6), 343–358. doi: 10.1007/BF00199415

Burnley, P. C. (1990). *The effect of nonhydrostatic stress on the olivine-spinel transformation in Mg_2GeO_4* (Ph.D. dissertat). U. of Calif., Davis.

Burnley, P. C. (1995). The fate of olivine in subducting slabs; a reconnaissance study. *American Mineralogist*, *80*(11-12), 1293–1301. doi: 10.2138/am-1995-11-1219

Burnley, P. C., Green, H. W., & Prior, D. J. (1991). Faulting associated with the olivine to spinel transformation in Mg_2GeO_4 and its implications for deep-focus earthquakes. *Journal of Geophysical Research*, *96*(B1), 425–443. doi: 10.1029/90JB01937

Capolungo, L., & Taupin, V. (2019). GD3: generalized discrete defect dynamics. *Materials Theory*, *3*(1), 2. doi: 10.1186/s41313-018-0013-9

Chen, L.-Q., & Khachaturyan, A. (1991). Computer simulation of structural transformations during precipitation of an ordered intermetallic phase. *Acta Metallurgica et Materialia*, *39*(11), 2533–2551. doi: 10.1016/0956-7151(91)90069-D

Dupas-Bruzek, C., Tingle, T. N., Green, H. W., Doukhan, N., & Doukhan, J. C. (1998). The rheology of olivine and spinel magnesium germanate (Mg_2GeO_4): TEM study of the defect microstructures. *Physics and Chemistry of Minerals*, *25*(7), 501–514. doi: https://doi.org/10.1007/s002690050142

Duyster, J., & Stöckhert, B. (2001). Grain boundary energies in olivine derived from

natural microstructures. *Contributions to Mineralogy and Petrology*, *140*(5), 567–576. doi: 10.1007/s004100000200

Eshelby, J. D. (1957). The determination of the elastic field of an ellipsoidal inclusion, and related problems. *Proceedings of the Royal Society of London. Series A. Mathematical and Physical Sciences*, *241*(1226), 376–396. doi: 10.1098/rspa.1957.0133

Evans, O., Spiegelman, M., & Kelemen, P. B. (2020). Phasefield modeling of reactiondriven cracking: determining conditions for extensive olivine serpentinization. *Journal of Geophysical Research: Solid Earth*, *125*(1), 1–21. doi: 10.1029/2019JB018614

Fitts, D. D. (1962). *Nonequilibrium Thermodynamics: A Phenomenological Theory of Irreversible Process in Fluid Systems*. Mc Graw-Hill Book.

Fix, G. (1983). Phase field models for free boundary problems. In A. Fasano & M. Primicerio (Eds.), *Free boundary problems: theory and applications* (II ed., pp. 580–589). Boston: Pitman Advanced Publishing Program.

Green, H. W. (2007). Shearing instabilities accompanying high-pressure phase transformations and the mechanics of deep earthquakes. *Proceedings of the National Academy of Sciences of the United States of America*, *104*(22), 9133–9138. doi: 10.1073/pnas.0608045104

Green, H. W., & Burnley, P. C. (1989). A new self-organizing mechanism for deep-focus earthquakes. *Nature*, *341*(6244), 733–737. doi: 10.1038/341733a0

Green, H. W., Young, T. E., Walker, D., & Scholz, C. H. (1990). Anticrack-associated faulting at very high pressure in natural olivine. *Nature*, *348*(6303), 720–722. doi: 10.1038/348720a0

Guo, X. H., Shi, S.-Q., & Ma, X. Q. (2005). Elastoplastic phase field model for microstructure evolution. *Applied Physics Letters*, *87*(22), 221910. doi: 10.1063/1.2138358

Hillert, M. (1975). Diffusion and interface control of reactions in alloys. *Metallurgical Transactions A*, *6*(1), 5–19. doi: 10.1007/BF02673664

Hirth, J. P., Hirth, G., & Wang, J. (2020). Disclinations and disconnections in minerals and metals. *Proceedings of the National Academy of Sciences of the United States of America*, *117*(1), 196–204. doi: 10.1073/pnas.1915140117

Hobbs, B. E., & Ord, A. (1988). Plastic instabilities: Implications for the origin

of intermediate and deep focus earthquakes. *Journal of Geophysical Research: Solid Earth*, *93*(B9), 10521–10540. doi: 10.1029/JB093iB09p10521

Ishii, T., & Ohtani, E. (2021). Dry metastable olivine and slab deformation in a wet subducting slab. *Nature Geoscience*, *14*(7), 526–530. doi: 10.1038/s41561-021-00756-7

Karato, S.-i., Riedel, M. R., & Yuen, D. A. (2001). Rheological structure and deformation of subducted slabs in the mantle transition zone: implications for mantle circulation and deep earthquakes. *Physics of the Earth and Planetary Interiors*, *127*(1-4), 83–108. doi: 10.1016/S0031-9201(01)00223-0

Kashchiev, D. (2000). *Nucleation: Basic Theory with Applications*. Boston: Butterworth-Heinemann.

Kawada, Y., Nagahama, H., & Nakamura, N. (2007). Time-scale invariances in preseismic electromagnetic radiation, magnetization and damage evolution of rocks. *Natural Hazards and Earth System Science*, *7*(5), 599–606. doi: 10.5194/nhess-7-599-2007

Kerschhofer, L., Dupas, C., Liu, M., Sharp, T. G., Durham, W. B., & Rubie, D. C. (1998). Polymorphic transformations between olivine, wadsleyite and ringwoodite: mechanisms of intracrystalline nucleation and the role of elastic strain. *Mineralogical Magazine*, *62*(5), 617–638. doi: 10.1180/002646198548016

Kerschhofer, L., Rubie, D., Sharp, T., McConnell, J., & Dupas-Bruzek, C. (2000). Kinetics of intracrystalline olivineringwoodite transformation. *Physics of the Earth and Planetary Interiors*, *121*(1-2), 59–76. doi: 10.1016/S0031-9201(00)00160-6

Kerschhofer, L., Sharp, T. G., & Rubie, D. C. (1996). Intracrystalline transformation of olivine to wadsleyite and ringwoodite under subduction zone conditions. *Science*, *274*(5284), 79–81. doi: 10.1126/science.274.5284.79

Khachaturian, A. G. (1983). *Theory of Structural Transformations in Solids*. United States: John Wiley and Sons.

Kim, S. G., Kim, D. I., Kim, W. T., & Park, Y. B. (2006). Computer simulations of two-dimensional and three-dimensional ideal grain growth. *Physical Review E - Statistical, Nonlinear, and Soft Matter Physics*, *74*(6), 1–14. doi: 10.1103/PhysRevE.74.061605

Kirby, S. H. (1983). Rheology of the lithosphere. *Reviews of Geophysics*, *21*(6), 1458. doi: 10.1029/RG021i006p01458

Koyama, T., & Onodera, H. (2003). Phase-field simulation of microstructure changes in Ni_2MnGa ferromagnetic alloy under external stress and magnetic fields. *Materials Transactions*, *44*(12), 2503–2508. doi: 10.2320/matertrans.44.2503

Kubo, T., Kaneshima, S., Torii, Y., & Yoshioka, S. (2009). Seismological and experimental constraints on metastable phase transformations and rheology of the Mariana slab. *Earth and Planetary Science Letters*, *287*(1-2), 12–23. doi: 10.1016/j.epsl.2009.07.028

Liebermann, R. C. (1975). Elasticity of olivine (α), beta (β), and spinel (γ) polymorphs of germanates and silicates. *Geophysical Journal of the Royal Astronomical Society*, *42*(3), 899–929. doi: 10.1111/j.1365-246X.1975.tb06458.x

Liu, M., Kerschhofer, L., Mosenfelder, J. L., & Rubie, D. C. (1998). The effect of strain energy on growth rates during the olivine-spinel transformation and implications for olivine metastability in subducting slabs. *Journal of Geophysical Research: Solid Earth*, *103*(B10), 23897–23909. doi: 10.1029/98JB00794

Lyakhovsky, V., Ben-Zion, Y., & Agnon, A. (1997). Distributed damage, faulting, and friction. *Journal of Geophysical Research B: Solid Earth*, *102*(12), 27635–27649. doi: 10.1029/97jb01896

Lyakhovsky, V., Podladchikov, Y., & Alexei, P. (1993). A rheological model of a fractured solid. *Tectonophysics*, *226*(1-4), 187–198. doi: 10.1016/0040-1951(93)90117-3

Majewski, E., & Teisseyre, R. (1998). Anticrack-associated faulting in deep subduction zones. *Physics and Chemistry of the Earth*, *23*(9-10), 1115–1122. doi: 10.1016/S0079-1946(98)00138-4

Meng, L., Ampuero, J.-P., & Bürgmann, R. (2014). The 2013 Okhotsk deep-focus earthquake: Rupture beyond the metastable olivine wedge and thermally controlled rise time near the edge of a slab. *Geophysical Research Letters*, *41*(11), 3779–3785. doi: 10.1002/2014GL059968

Meyers, M. A., Armstrong, R. W., & Kirchner, H. O. K. (1999). *Mechanics and Materials: Fundamentals and Linkages*. Wiley.

Miehe, C., Hofacker, M., Schänzel, L. M., & Aldakheel, F. (2015). Phase field modeling of fracture in multi-physics problems. Part II. Coupled brittle-to-ductile

failure criteria and crack propagation in thermo-elastic-plastic solids. *Computer Methods in Applied Mechanics and Engineering*, *294*, 486–522. doi: 10.1016/j.cma.2014.11.017

Miyazaki, T., Nakamura, K., & Mori, H. (1979). Experimental and theoretical investigations on morphological changes of γ' precipitates in Ni -Al single crystals during uniaxial stress-annealing. *Journal of Materials Science*, *14*(8), 1827–1837. doi: 10.1007/BF00551021

Mosenfelder, J. L., Rubie, D. C., Marton, F. C., Ross, C. R., & Kerschhofer, L. (2001). Experimental constraints on the depth of olivine metastability in subducting lithosphere. *Physics of the Earth and Planetary Interiors*, *127*(1-4), 165–180. doi: 10.1016/S0031-9201(01)00226-6

Muto, J., Nagahama, H., Miura, T., & Arakawa, I. (2007). Frictional discharge at fault asperities: Origin of fractal seismo-electromagnetic radiation. *Tectonophysics*, *431*(1-4), 113–122. doi: 10.1016/j.tecto.2006.05.045

Nabarro, F. R. N. (1940). The strains produced by precipitation in alloys. *Proceedings of the Royal Society of London. Series A, Mathematical and Physical Sciences*, *175*(963), 519–538.

Ogawa, M. (1987). Shear instability in a viscoelastic material as the cause of deep focus earthquakes. *Journal of Geophysical Research: Solid Earth*, *92*(B13), 13801–13810. doi: 10.1029/JB092iB13p13801

Pineau, A. (1976). Influence of uniaxial stress on the morphology of coherent precipitates during coarseningelastic energy considerations. *Acta Metallurgica*, *24*(6), 559–564. doi: 10.1016/0001-6160(76)90101-2

Read, W. T., & Shockley, W. (1950). Dislocation models of crystal grain boundaries. *Physical Review*, *78*(3), 275–289. doi: 10.1103/PhysRev.78.275

Riggs, E. M., & Green, H. W. (2005). A new class of microstructures which lead to transformation-induced faulting in magnesium germanate. *Journal of Geophysical Research: Solid Earth*, *110*(3), 1–15. doi: 10.1029/2004JB003391

Ross, N. L., & Navrotsky, A. (1987). The Mg_2GeO_4 olivine-spinel phase transition. *Physics and Chemistry of Minerals*, *14*(5), 473–481. doi: 10.1007/BF00628825

Roy, D. M., & Roy, R. (1954). An experimental study of the formation and properties of synthetic serpentines and related layer silicate minerals. *American Min-*

eralogist, *39*(53), 957–975.

Rubie, D. C. (1984). The olivine spinel transformation and the rheology of subducting lithosphere. *Nature*, *308*(5959), 505–508. doi: 10.1038/308505a0

Sawa, S., Miyajima, N., Muto, J., & Nagahama, H. (2021). Strain-induced partial serpentinization of germanate olivine with a small amount of water. *American Mineralogist*, 1–36. doi: 10.2138/am-2021-7735

Sawa, S., Muto, J., Miyajima, N., Shiraishi, R., Kido, M., & Nagahama, H. (2021). Strain localization bands in fine-grained aggregates of germanate olivine and pyroxene deformed by a Griggs type apparatus. *International Journal of Rock Mechanics and Mining Sciences*, *144*, 104812. doi: 10.1016/j.ijrmms.2021.104812

Schneider, D., Schoof, E., Huang, Y., Selzer, M., & Nestler, B. (2016). Phase-field modeling of crack propagation in multiphase systems. *Computer Methods in Applied Mechanics and Engineering*, *312*, 186–195. doi: 10.1016/j.cma.2016.04.009

Schubnel, A., Brunet, F., Hilairet, N., Gasc, J., Wang, Y., & Green, H. W. (2013). Deep-focus earthquake analogs recorded at high pressure and temperature in the laboratory. *Science*, *341*(6152), 1377–1380. doi: 10.1126/science.1240206

Shi, F., Zhang, J., Xia, G., Jin, Z., & Green, H. W. (2015). Rheology of Mg_2GeO_4 olivine and spinel harzburgite: Implications for Earth's mantle transition zone. *Geophysical Research Letters*, *42*(7), 2212–2218. doi: 10.1002/2015GL063316

Shimokawabe, T., Takaki, T., Endo, T., Yamanaka, A., Maruyama, N., Aoki, T., ... Matsuoka, S. (2011). Peta-scale phase-field simulation for dendritic solidification on the TSUBAME 2.0 supercomputer. *Proceedings of 2011 International Conference for High Performance Computing, Networking, Storage and Analysis*, 1–11. doi: 10.1145/2063384.2063388

Steinbach, I., & Apel, M. (2006). Multi phase field model for solid state transformation with elastic strain. *Physica D: Nonlinear Phenomena*, *217*(2), 153–160. doi: 10.1016/j.physd.2006.04.001

Steinbach, I., & Pezzolla, F. (1999). A generalized field method for multiphase transformations using interface fields. *Physica D: Nonlinear Phenomena*, *134*(4), 385–393. doi: 10.1016/S0167-2789(99)00129-3

Steinbach, I., Pezzolla, F., Nestler, B., Seeßelberg, M., Prieler, R., Schmitz, G., &

Rezende, J. (1996). A phase field concept for multiphase systems. *Physica D: Nonlinear Phenomena*, *94*(3), 135–147. doi: 10.1016/0167-2789(95)00298-7

Tajima, F., Yoshida, M., & Ohtani, E. (2015). Conjecture with water and rheological control for subducting slab in the mantle transition zone. *Geoscience Frontiers*, *6*(1), 79–93. doi: 10.1016/j.gsf.2013.12.005

Takaki, T., Hirouchi, T., Hisakuni, Y., Yamanaka, A., & Tomita, Y. (2008). Multi-phase-field model to simulate microstructure evolutions during dynamic recrystallization. *MATERIALS TRANSACTIONS*, *49*(11), 2559–2565. doi: 10.2320/matertrans.MB200805

Takaki, T., Hisakuni, Y., Hirouchi, T., Yamanaka, A., & Tomita, Y. (2009). Multi-phase-field simulations for dynamic recrystallization. *Computational Materials Science*, *45*(4), 881–888. doi: 10.1016/j.commatsci.2008.12.009

Takaki, T., & Tomita, Y. (2010). Static recrystallization simulations starting from predicted deformation microstructure by coupling multi-phase-field method and finite element method based on crystal plasticity. *International Journal of Mechanical Sciences*, *52*(2), 320–328. doi: 10.1016/j.ijmecsci.2009.09.037

Takaki, T., Yoshimoto, C., Yamanaka, A., & Tomita, Y. (2014). Multiscale modeling of hot-working with dynamic recrystallization by coupling microstructure evolution and macroscopic mechanical behavior. *International Journal of Plasticity*, *52*, 105–116. doi: 10.1016/j.ijplas.2013.09.001

Tingle, T. N., Green, H. W., Scholz, C. H., & Koczynski, T. A. (1993). The rheology of faults triggered by the olivine-spinel transformation in Mg_2GeO_4 and its implications for the mechanism of deep-focus earthquakes. *Journal of Structural Geology*, *15*(9-10), 1249–1256. doi: 10.1016/0191-8141(93)90167-9

Tsukada, Y., Murata, Y., Koyama, T., Miura, N., & Kondo, Y. (2011). Creep deformation and rafting in nickel-based superalloys simulated by the phase-field method using classical flow and creep theories. *Acta Materialia*, *59*(16), 6378–6386. doi: 10.1016/j.actamat.2011.06.050

Vaughan, P. J., & Coe, R. S. (1981). Creep mechanism in Mg_2GeO_4: Effects of a phase transition. *Journal of Geophysical Research*, *86*(B1), 389. doi: 10.1029/JB086iB01p00389

Vaughan, P. J., Green, H. W., & Coe, R. S. (1982, jul). Is the olivinespinel phase transformation martensitic? *Nature*, *298*(5872), 357–358. doi:

10.1038/298357a0

Volterra, V. (1907). Sur l'équilibre des corps élastiques multiplement connexes. *Annales Scientifiques de l'École Normale Supérieure*, *24*, 401–517.

Von Dreele, R., Navrotsky, A., & Bowman, A. (1977). Refinement of the crystal structure of Mg_2GeO_4 spinel. *Acta Crystallographica Section B Structural Crystallography and Crystal Chemistry*, *33*(7), 2287–2288. doi: 10.1107/S056774087700822X

Wang, Y., & Khachaturyan, A. G. (1997). Three-dimensional field model and computer modeling of martensitic transformations. *Acta Metallurgica*, *45*(2), 759–773. doi: https://doi.org/10.1016/S1359-6454(96)00180-2

Wang, Y., Zhu, L., Shi, F., Schubnel, A., Hilairet, N., Yu, T., ... Brunet, F. (2017). A laboratory nanoseismological study on deep-focus earthquake micromechanics. *Science Advances*, *3*(7), e1601896. doi: 10.1126/sciadv.1601896

Weidner, D. J., & Hamaya, N. (1983). Elastic properties of the olivine and spinel polymorphs of Mg_2GeO_4, and evaluation of elastic analogues. *Physics of the Earth and Planetary Interiors*, *33*(4), 275–283. doi: 10.1016/0031-9201(83)90045-6

Wheeler, A., Murray, B., & Schaefer, R. (1993). Computation of dendrites using a phase field model. *Physica D: Nonlinear Phenomena*, *66*(1), 243–262. doi: 10.1016/0167-2789(93)90242-S

Yamanaka, A., Takaki, T., & Tomita, Y. (2008). Elastoplastic phase-field simulation of self and plastic accommodations in Cubic tetragonal martensitic transformation. *Materials Science and Engineering A*, *491*(1-2), 378–384. doi: 10.1016/j.msea.2008.02.035

Yamanaka, A., Takaki, T., & Tomita, Y. (2010). Elastoplastic phase-field simulation of martensitic transformation with plastic deformation in polycrystal. *International Journal of Mechanical Sciences*, *52*(2), 245–250. doi: 10.1016/j.ijmecsci.2009.09.020

Yamazaki, D., Inoue, T., Okamoto, M., & Irifune, T. (2005). Grain growth kinetics of ringwoodite and its implication for rheology of the subducting slab. *Earth and Planetary Science Letters*, *236*(3-4), 871–881. doi: 10.1016/j.epsl.2005.06.005

Yang, S., Ukrainczyk, N., Caggiano, A., & Koenders, E. (2021). Numerical phase-

field model validation for dissolution of minerals. *Applied Sciences*, *11*(6), 2464. doi: 10.3390/app11062464

Yeddu, H. K., Malik, A., Gren, J., Amberg, G., & Borgenstam, A. (2012). Three-dimensional phase-field modeling of martensitic microstructure evolution in steels. *Acta Materialia*, *60*(4), 1538–1547. doi: 10.1016/j.actamat.2011.11.039

Zhan, Z. (2017). GutenbergRichter law for deep earthquakes revisited: A dual-mechanism hypothesis. *Earth and Planetary Science Letters*, *461*, 1–7. doi: 10.1016/j.epsl.2016.12.030

Zhan, Z., Kanamori, H., Tsai, V. C., Helmberger, D. V., & Wei, S. (2014). Rupture complexity of the 1994 Bolivia and 2013 Sea of Okhotsk deep earthquakes. *Earth and Planetary Science Letters*, *385*, 89–96. doi: 10.1016/j.epsl.2013.10.028

Figure 1.

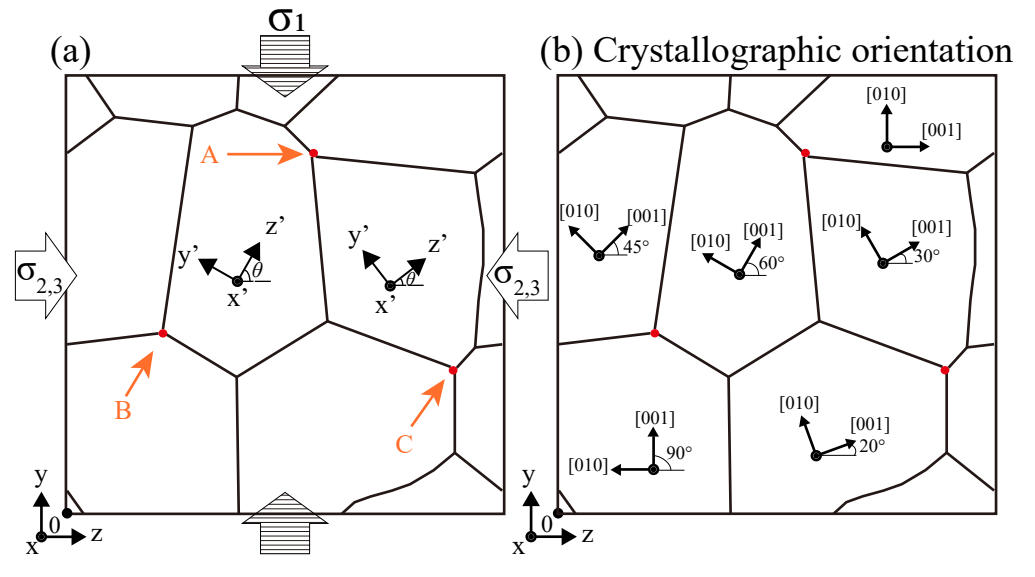
(a)
σ1
σ2,3
σ2,3
A
B
C
y'
z'
x'
θ
y
z
x
0
(b) Crystallographic orientation
[010]
[001]
45°
60°
30°
90°
20°

Figure 2.

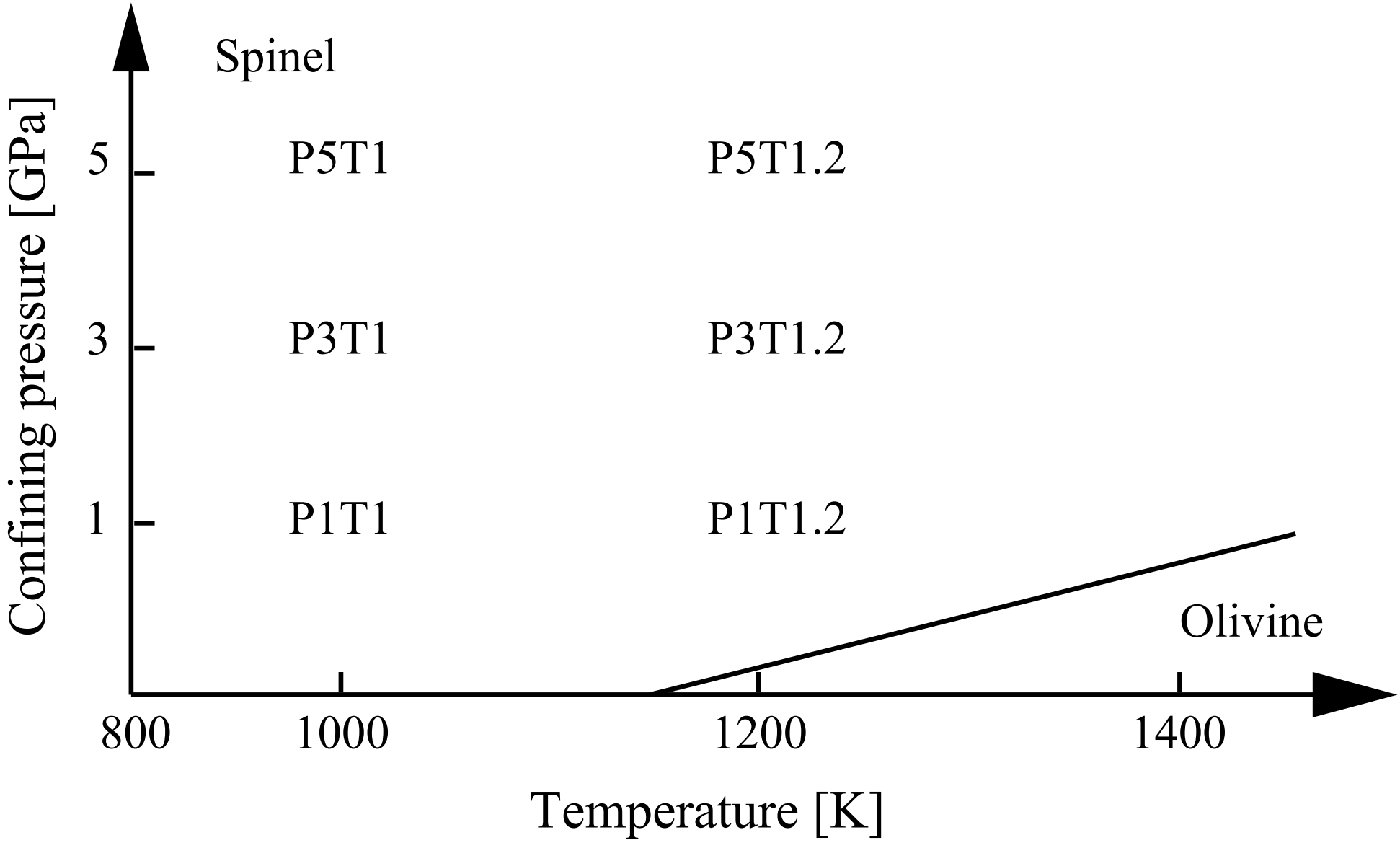
Spinel
5
3
1
P5T1
P5T1.2
P3T1
P3T1.2
P1T1
P1T1.2
Olivine
Confining pressure [GPa]
800
1000
1200
1400
Temperature [K]

Figure 3.

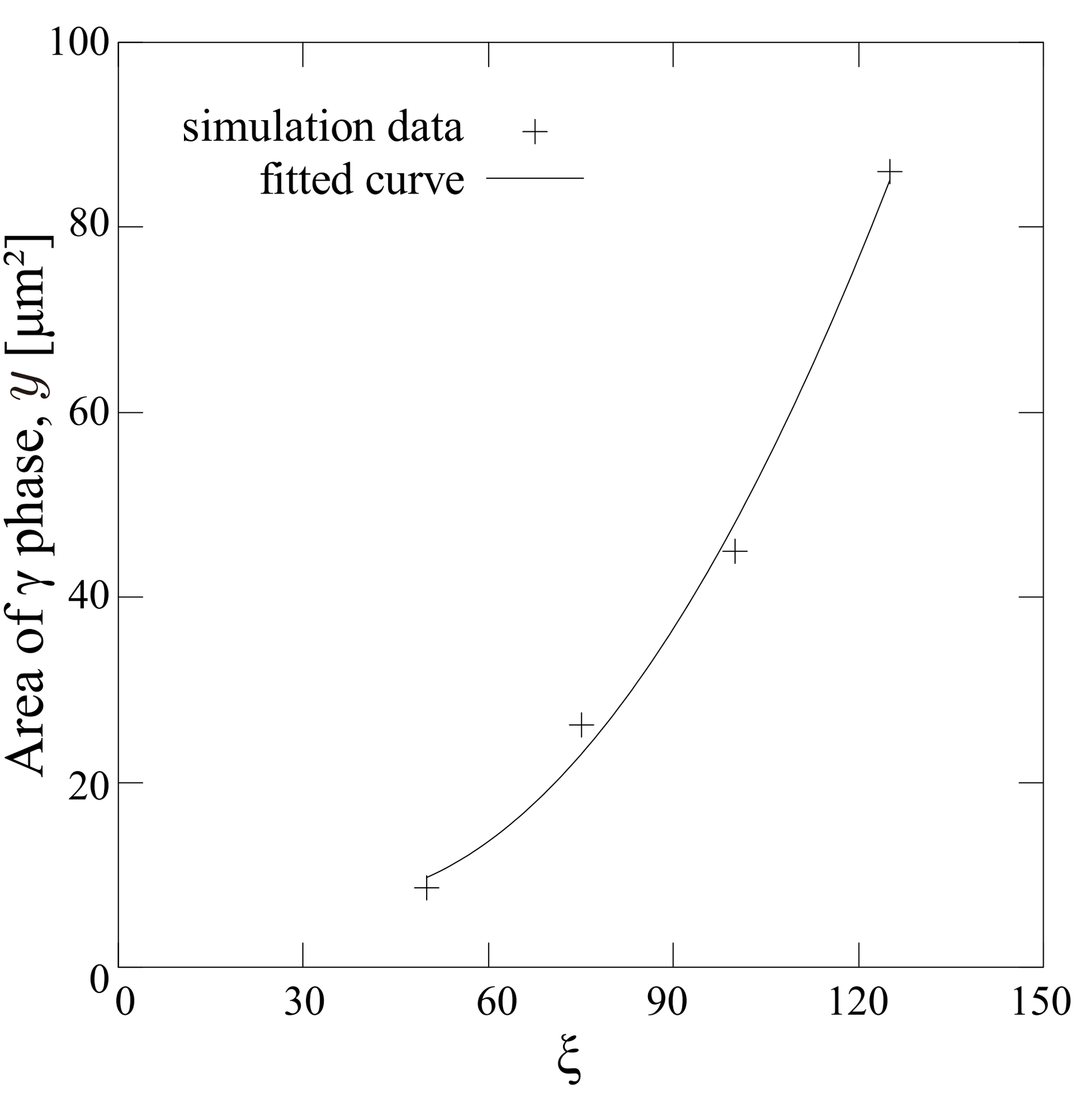
simulation data
fitted curve
Area of γ phase, y [μm^2]
ξ
0
20
40
60
80
100
0
30
60
90
120
150

Figure 4.

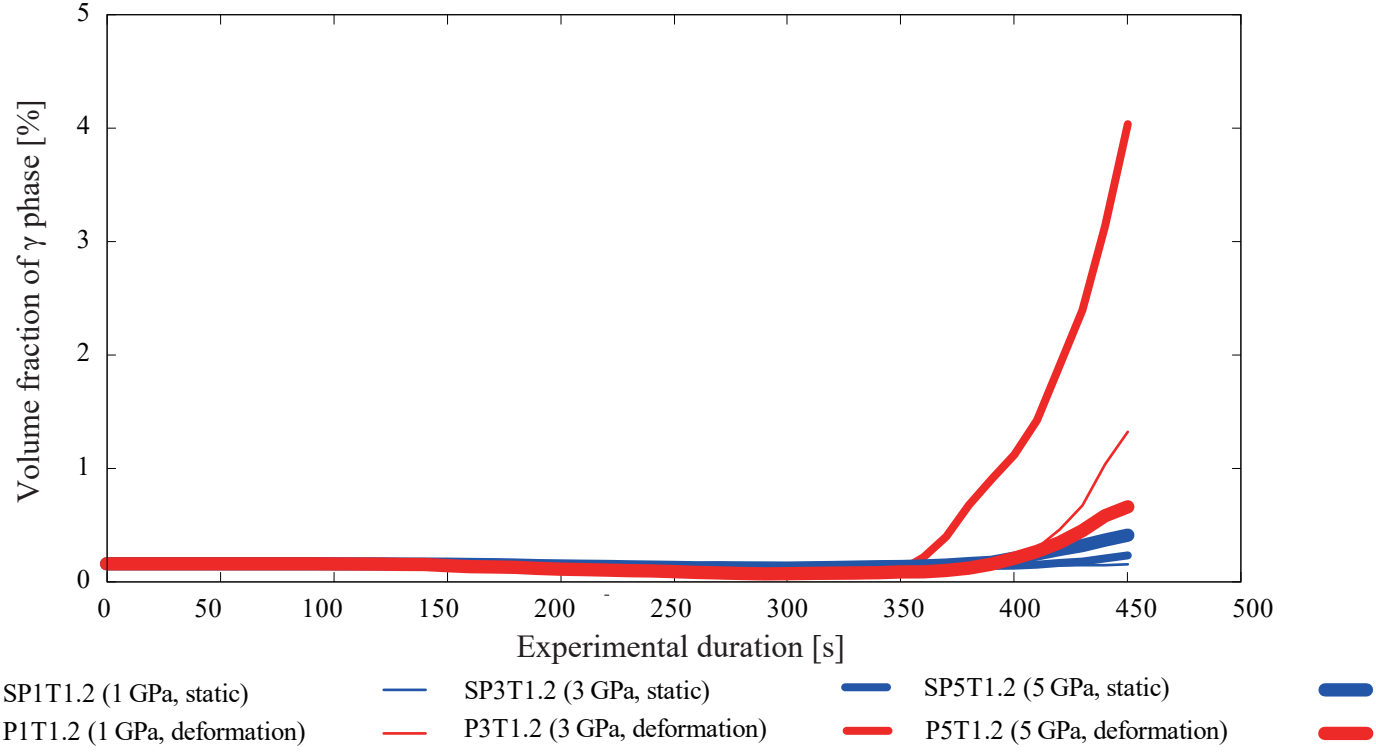
Volume fraction of γ phase [%]
0
1
2
3
4
5
0
50
100
150
200
250
300
350
400
450
500
Experimental duration [s]
SP1T1.2 (1 GPa, static)
P1T1.2 (1 GPa, deformation)
SP3T1.2 (3 GPa, static)
P3T1.2 (3 GPa, deformation)
SP5T1.2 (5 GPa, static)
P5T1.2 (5 GPa, deformation)

Figure 5.

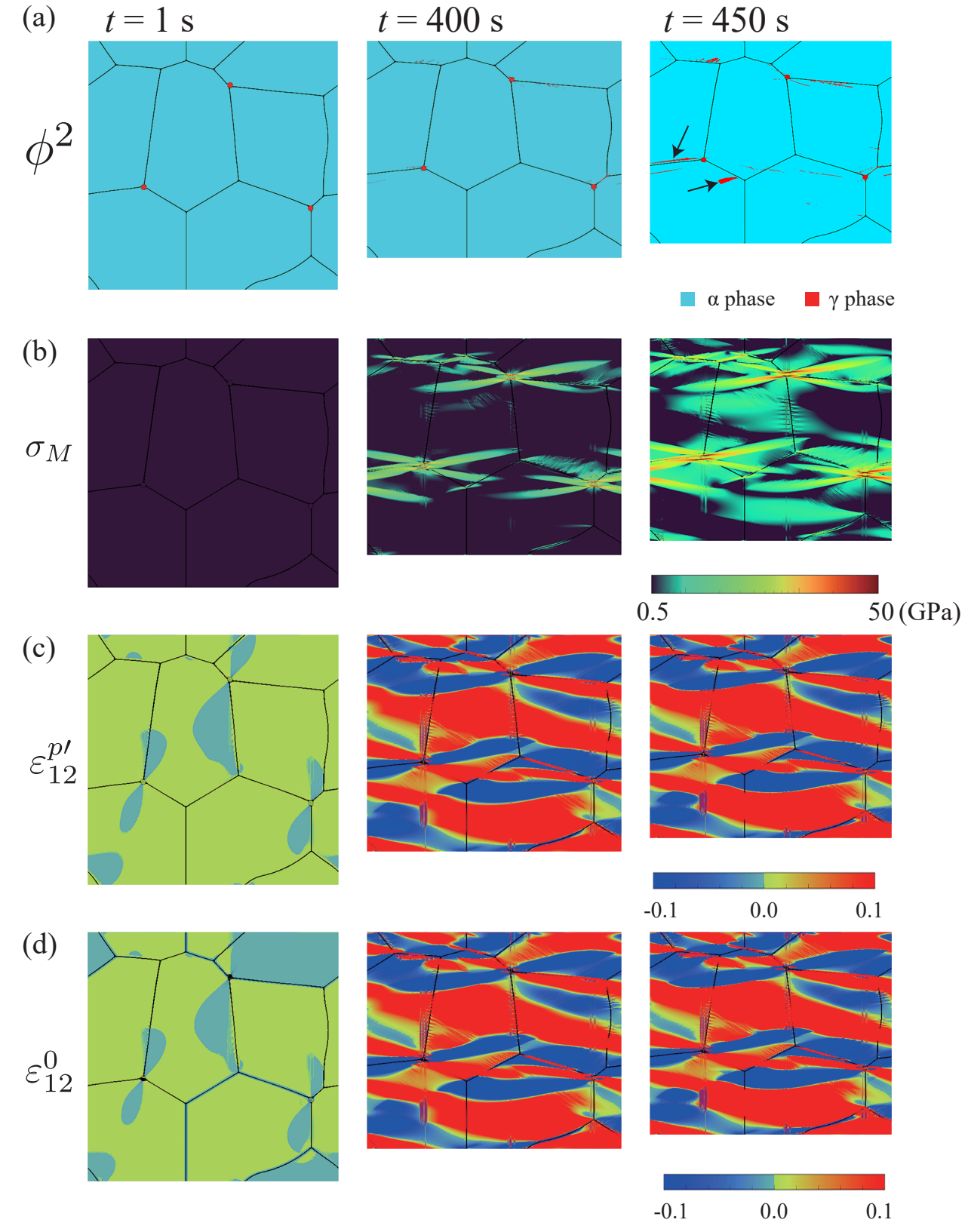
P1T1.2 (P = 1 GPa, T = 1200 K, deformation experiment)
(a)
t = 1 s
t = 400 s
t = 450 s
ϕ^2
α phase
γ phase
(b)
σ_M
0.5
50 (GPa)
(c)
$\varepsilon_{12}^{p\prime}$
-0.1
0.0
0.1
(d)
ε_{12}^{0}
-0.1
0.0
0.1

Figure 6.

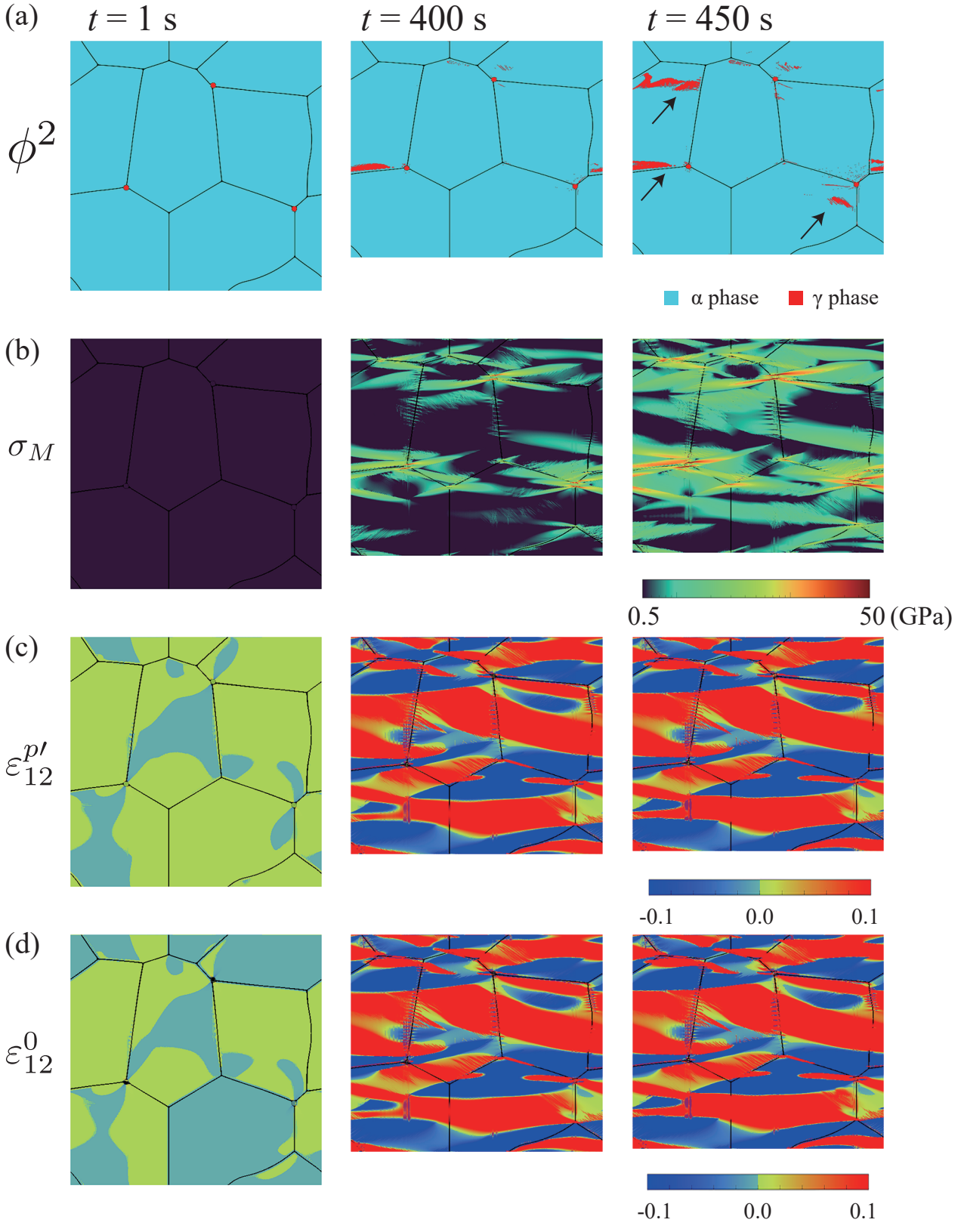
P3T1.2 (P = 3 GPa, T = 1200 K, deformation experiment)
(a)
t = 1 s
t = 400 s
t = 450 s
ϕ^2
α phase
γ phase
(b)
σ_M
0.5
50 (GPa)
(c)
ε_{12}^{pl}
-0.1
0.0
0.1
(d)
ε_{12}^{0}
-0.1
0.0
0.1

Figure 7.

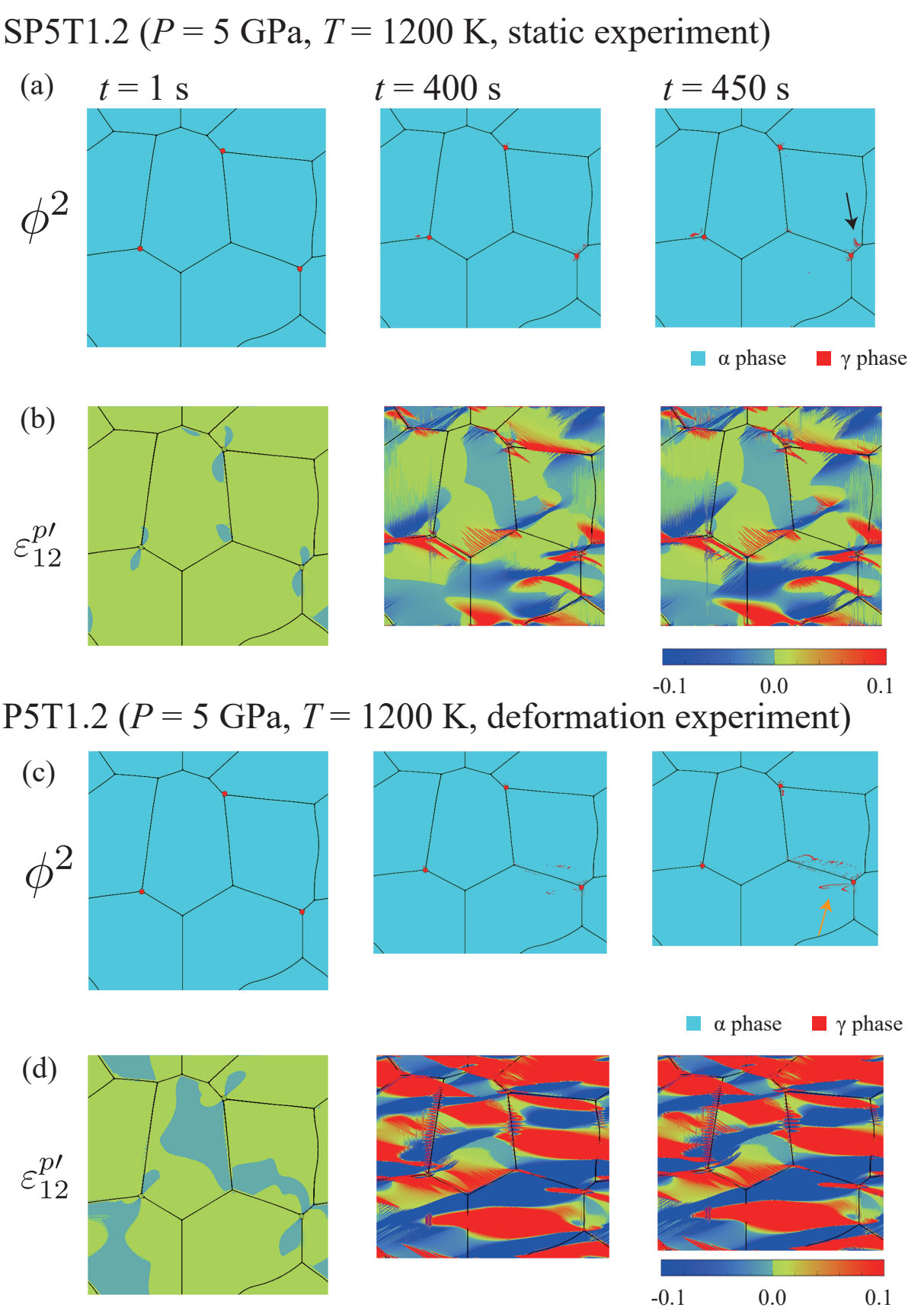
SP5T1.2 (P = 5 GPa, T = 1200 K, static experiment)
(a)
t = 1 s
t = 400 s
t = 450 s
ϕ^2
α phase
γ phase
(b)
$\varepsilon_{12}^{p\prime}$
-0.1
0.0
0.1
P5T1.2 (P = 5 GPa, T = 1200 K, deformation experiment)
(c)
ϕ^2
α phase
γ phase
(d)
$\varepsilon_{12}^{p\prime}$
-0.1
0.0
0.1

Figure 8.

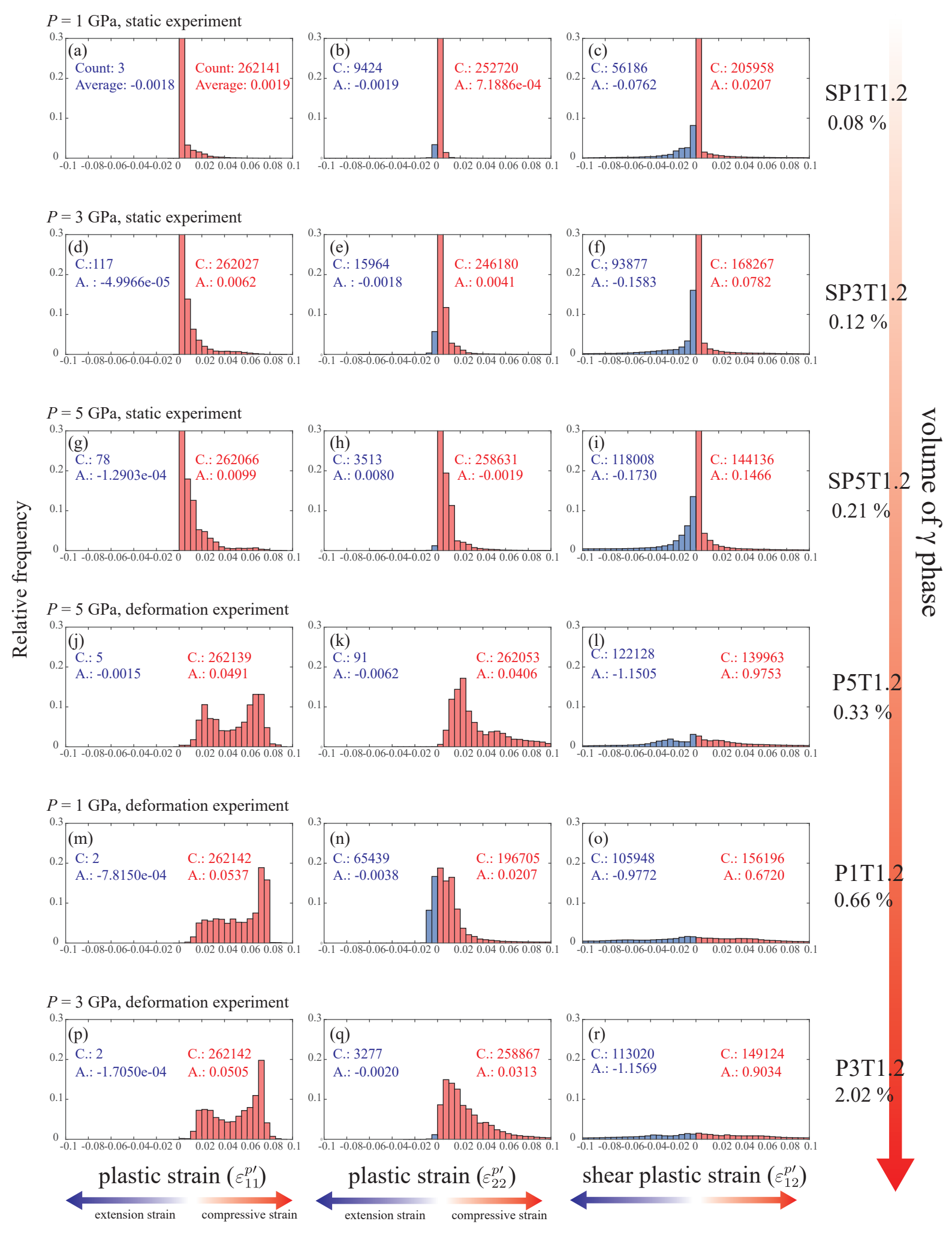
P = 1 GPa, static experiment
(a)
Count: 3
Average: -0.0018
Count: 262141
Average: 0.0019
(b)
C.: 9424
A.: -0.0019
C.: 252720
A.: 7.1886e-04
(c)
C.: 56186
A.: -0.0762
C.: 205958
A.: 0.0207
SP1T1.2
0.08 %
P = 3 GPa, static experiment
(d)
C.:117
A. : -4.9966e-05
C.: 262027
A.: 0.0062
(e)
C.: 15964
A. : -0.0018
C.: 246180
A.: 0.0041
(f)
C.; 93877
A.: -0.1583
C.: 168267
A.: 0.0782
SP3T1.2
0.12 %
P = 5 GPa, static experiment
(g)
C.: 78
A.: -1.2903e-04
C.: 262066
A.: 0.0099
(h)
C.: 3513
A.: 0.0080
C.: 258631
A.: -0.0019
(i)
C.: 118008
A.: -0.1730
C.: 144136
A.: 0.1466
SP5T1.2
0.21 %
P = 5 GPa, deformation experiment
(j)
C.: 5
A.: -0.0015
C.: 262139
A.: 0.0491
(k)
C.: 91
A.: -0.0062
C.: 262053
A.: 0.0406
(l)
C.: 122128
A.: -1.1505
C.: 139963
A.: 0.9753
P5T1.2
0.33 %
P = 1 GPa, deformation experiment
(m)
C: 2
A.: -7.8150e-04
C.: 262142
A.: 0.0537
(n)
C.: 65439
A.: -0.0038
C.: 196705
A.: 0.0207
(o)
C.: 105948
A.: -0.9772
C.: 156196
A.: 0.6720
P1T1.2
0.66 %
P = 3 GPa, deformation experiment
(p)
C.: 2
A.: -1.7050e-04
C.: 262142
A.: 0.0505
(q)
C.: 3277
A.: -0.0020
C.: 258867
A.: 0.0313
(r)
C.: 113020
A.: -1.1569
C.: 149124
A.: 0.9034
P3T1.2
2.02 %
Relative frequency
volume of γ phase
plastic strain ($\varepsilon_{11}^{p\prime}$)
plastic strain ($\varepsilon_{22}^{p\prime}$)
shear plastic strain ($\varepsilon_{12}^{p\prime}$)
extension strain
compressive strain
extension strain
compressive strain